

Adaptive broadening to improve spectral resolution in the numerical renormalization group

Seung-Sup B. Lee* and Andreas Weichselbaum†

*Physics Department, Arnold Sommerfeld Center for Theoretical Physics and Center for NanoScience,
Ludwig-Maximilians-Universität München, Theresienstraße 37, 80333 München, Germany*

(Dated: August 25, 2021)

We propose an adaptive scheme of broadening the discrete spectral data from numerical renormalization group (NRG) calculations to improve the resolution of dynamical properties at finite energies. While the conventional scheme overbroadens narrow features at large frequency by broadening discrete weights with constant width in log-frequency, our scheme broadens each discrete contribution individually based on its sensitivity to a z -shift in the logarithmic discretization intervals. We demonstrate that the adaptive broadening better resolves various features in non-interacting and interacting models at comparable computational cost. The resolution enhancement is more significant for coarser discretization as typically required in multi-band calculations. At low frequency below the energy scale of temperature, the discrete NRG data necessarily needs to be broadened on a linear scale. Here we provide a method that minimizes transition artefacts in between these broadening kernels.

I. INTRODUCTION

The numerical renormalization group (NRG) is a non-perturbative method to solve quantum impurity problems^{1,2}, with applications ranging from actual quantum impurities in mesoscopic systems to self-consistent impurity models in dynamical mean-field theory (DMFT)³⁻⁵. Owing to using a logarithmic discretization grid, the NRG has major advantages in calculating dynamical properties. Most importantly, it can reach arbitrarily low temperatures at comparable computational cost, and satisfies the Friedel sum rule at temperature $T = 0^+$ generally within 1% deviation.

The above benefits come at the cost that NRG only provides finite spectral resolution of dynamical properties at finite frequencies. With many-body eigenstates $H|E_i\rangle = E_i|E_i\rangle$, dynamical properties of the impurity such as the local density of states can be written in Lehmann representation as

$$A(\omega) = \sum_{ij} A_{ij} \delta(\omega - E_j + E_i) \quad (1)$$

where we use $\hbar = k_B = 1$ in this paper, throughout. According to the exponential coarse-graining in energy, the conventional approach^{6,7} broadens every discrete spectral weight A_{ij} at $|\omega| > T$ with constant width σ in log-frequency or, equivalently, constant width-to-position ratio in linear frequency. As a consequence, sharp features at finite frequency either show artificial oscillatory behavior for too small σ or are overbroadened otherwise. This oscillatory behavior is also inherited by static observables e.g. as function of temperature. A standard prescription to deal with this situation is z -averaging, which averages the discrete spectral data over n_z logarithmic grids (shifted relative to each other by a parameter z), allowing the broadening width proportional to $1/n_z$ ⁸⁻¹⁰. However, z -averaging is inherently sensitive to the precise treatment of the band edges¹⁰ in that state space truncation inevitably introduces slight inequivalences for differ-

ent z -shifts. Eventually, this limits resolution. Therefore besides z -averaging, it is desirable to have a broadening scheme that incorporates more information about the spectral data to be broadened.¹¹

In this work, we propose an adaptive broadening scheme that systematically improves resolution of dynamical properties at finite frequencies. For $|\omega| > T$, contrary to the conventional broadening scheme of constant $\sigma_{(ij)}$ for all weights A_{ij} , we determine the broadening width σ_{ij} individually for each A_{ij} from the sensitivity of its position $\omega_{ij} = E_j - E_i$ to z -shift, i.e., $\sigma_{ij} \propto d \log |\omega_{ij}| / dz$. For $|\omega| < T$, the curve is further convolved with a kernel of width $\gamma < T$ on a linear frequency scale to ensure smooth behavior across $\omega = 0$. We propose a generic scheme to minimize γ while maintaining a smooth curve for $|\omega| \lesssim T$ without artificial features at $|\omega| \sim T$. We show that this scheme captures, for example, narrow single-particle resonances in non-interacting models by using a clearly reduced number of z -shifts. For interacting models, such as the Kondo model and the single-impurity Anderson model (SIAM), the adaptive broadening better resolves sharp band edges, Hubbard side peaks, or the splitting of Kondo peak by magnetic field.

This paper is organized as follows. In Sec. II, we briefly review how discrete spectral data of the dynamical properties is obtained within the NRG framework. In Sec. III, we present our adaptive broadening scheme. In Sec. IV, we compare the adaptive scheme with the conventional one, by applying them to various systems at $T = 0$. In Sec. V, we apply the adaptive scheme at finite T .

II. DISCRETE DATA OF DYNAMICAL PROPERTIES BY NRG

A. Model Hamiltonians

The generic Hamiltonian of a quantum impurity problem can be written as

$$H = \underbrace{H_{\text{imp}}(\{d_\nu\}) + H_{\text{cpl}}(\{d_\nu, c_{e\nu}\})}_{\equiv H_0} + H_{\text{bath}}(\{c_{e\nu}\}), \quad (2)$$

where ν is an index of constituent particle species (e.g. spin, flavor, channel), d_ν is the annihilation operator at the impurity, and $c_{e\nu}$ annihilates a bath particle with energy ϵ in the bath, satisfying $\{c_{e\nu}, c_{e'\nu'}^\dagger\} = \delta(\epsilon - \epsilon')\delta_{\nu\nu'}$. While different particle species interact locally within the impurity Hamiltonian or the coupling, $H_0 \equiv H_{\text{imp}} + H_{\text{cpl}}$, the bath Hamiltonian is quadratic,

$$H_{\text{bath}} = \sum_\nu \int d\epsilon \epsilon c_{e\nu}^\dagger c_{e\nu}. \quad (3)$$

In the case of the SIAM, its coupling H_{cpl} to the impurity is also quadratic and given by,

$$H_{\text{cpl}}^{\text{SIAM}} = \sum_\nu \int d\epsilon \sqrt{\frac{\Gamma_\nu(\epsilon)}{\pi}} (d_\nu^\dagger c_{e\nu} + c_{e\nu}^\dagger d_\nu), \quad (4)$$

where $\Gamma_\nu(\epsilon)$ is an energy-dependent hybridization between the impurity and the bath, and $\nu \in \{\uparrow, \downarrow\}$ the electronic spin. Throughout this work we use a species-independent hybridization $\Gamma_\nu(\epsilon) = \Gamma(\epsilon) = \Gamma\Theta(D - |\epsilon|)$ and choose the half-bandwidth D as unit of energy, i.e. $D := 1$. In the SIAM, the impurity is a single spinful electronic site with Coulomb interaction,

$$H_{\text{imp}}^{\text{SIAM}} = U n_{d\uparrow} n_{d\downarrow} + \epsilon_d n_d + B S_{d,z}, \quad (5)$$

where $n_{d\nu} \equiv d_\nu^\dagger d_\nu$, $n_d \equiv n_{d\uparrow} + n_{d\downarrow}$ counts the number of particles on the impurity, $S_{d,z} \equiv \frac{1}{2}(n_{d\uparrow} - n_{d\downarrow})$ is the spin operator, U the Coulomb interaction strength, ϵ_d the energy of the single-particle level, and B the Zeeman splitting due to a magnetic field in z -direction. Here we consider the particle-hole symmetric case $\epsilon_d = -U/2$.

The Kondo model is the projection of the particle-hole symmetric SIAM onto the subspace where only one electron occupies the impurity, in the limit $U \gg \Gamma, D$. A Schrieffer-Wolff transformation results in

$$H_0^{\text{Kondo}} = J \vec{S}_d \cdot \vec{S}_0 + B S_{d,z}, \quad (6)$$

with $\vec{S}_0 \equiv \int_{-D}^D d\epsilon \int_{-D}^D d\epsilon' \sum_{\nu, \nu'=\uparrow, \downarrow} c_{e\nu}^\dagger [\vec{\sigma}]_{\nu\nu'} c_{e'\nu'}$ the spin of the bath site at the location of the impurity, $\vec{\sigma}$ the Pauli spin matrices, \vec{S}_d the impurity spin operator, and $J \simeq 8\Gamma D/\pi U > 0$.

B. NRG discretization

A quantum impurity problem considers a localized impurity coupled to a non-interacting bath of half-bandwidth. In units of $D = 1$, its continuous energies in $[-1, 1]$ are discretized into logarithmic intervals split at $\pm\Lambda^{-k+1-z}$ for $k = 1, 2, \dots$ where $\Lambda > 1$ is logarithmic discretization parameter and $z \in (0, 1]$ a discretization shift⁸⁻¹⁰ referred to as z -shift. Here we choose $\Lambda = 2$ and $z \in \{1/n_z, 2/n_z, \dots, 1\}$. This coarse-graining is followed by an exact mapping onto the discrete Wilson chain,^{1,2} with exponentially decaying hopping amplitudes, i.e. $t_n \propto \Lambda^{-n/2}$. This introduces energy scale separation and thus justifies iterative diagonalization of the Wilson chain.

After discretization and mapping onto the Wilson chain, the SIAM becomes

$$H_N^{\text{SIAM}}(z) = \underbrace{H_{\text{imp}}^{\text{SIAM}} + H_{\text{cpl}}^{\text{SIAM}}}_{\equiv H_0^{\text{SIAM}}} + H_N^{\text{bath}}(z), \quad (7)$$

now with

$$H_{\text{cpl}}^{\text{SIAM}} = \sum_{\nu=\uparrow, \downarrow} t_0 (d_\nu^\dagger f_{0\nu} + \text{H.c.}) \quad (8)$$

$$H_N^{\text{bath}}(z) = \sum_{n=1}^N \sum_{\nu=\uparrow, \downarrow} t_n^{(z)} (f_{n-1, \nu}^\dagger f_{n\nu} + \text{H.c.}). \quad (9)$$

where $t_0 = \sqrt{2\Gamma D/\pi}$ is z -independent, and where $f_{n\nu}$ annihilates the electron at the chain site $n = 0, 1, 2, \dots$ with spin ν . By construction, the Kondo model maps onto a similar chain geometry,

$$H_N^{\text{Kondo}}(z) = H_0^{\text{Kondo}} + H_N^{\text{bath}}(z), \quad (10)$$

with H_0^{Kondo} as in Eq. (6), but now with $\vec{S}_0 \equiv \sum_{\nu, \nu'=\uparrow, \downarrow} f_{0\nu}^\dagger [\vec{\sigma}]_{\nu\nu'} f_{0\nu'}$. Contrary to the original continuous Hamiltonian, the discrete Hamiltonians in Eqs. (7) and (10) depend on z , due to the z -dependence of discretized bath H_N^{bath} .

C. Dynamical properties

Based on the argument of energy scale separation, NRG proceeds with iterative diagonalization of the Wilson chain. This generates a complete set of well-approximated energy eigenstates $\{|E_i^{(z)}\rangle\}$ of the full chain.^{12,13} Having the energy eigenstates $\{|E_i^{(z)}\rangle\}$, the impurity's dynamics at finite temperature is described by local correlation functions in the Lehmann representation^{2,6,13,14} [see also Eq. (1)],

$$\begin{aligned} A_z^{\text{disc}}(\omega) &= -\frac{1}{\pi} \text{Im} \langle O || O^\dagger \rangle_\omega \\ &= -\frac{1}{\pi} \text{Im} \int dt e^{i\omega t} (-i\Theta(t) \langle [O(t), O^\dagger]_{\pm} \rangle) \end{aligned}$$

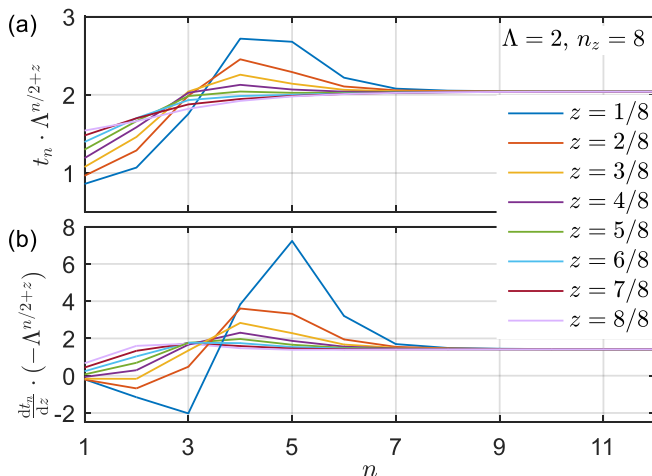


FIG. 1. (a) The hopping amplitudes $t_n^{(z)}$ vs. Wilson shell index n and (b) their derivatives dt_n/dz (obtained numerically using $\delta z = 0.01/n_z$), for the hybridization $\Gamma(\epsilon) = \Gamma\Theta(D - |\epsilon|)$ in units of half-bandwidth, i.e. $D = 1$. Since $t_{n=0}$ is independent of z , only data for $n > 0$ is shown, which itself is independent of the value of Γ . For large $n \gtrsim 8$, t_n and dt_n/dz follow an exponential scaling, i.e., $t_n \simeq \Lambda^{-z} \Lambda^{(1-n)/2} (\Lambda - 1) / \log \Lambda$ and $(dt_n/dz)/t_n = d \log(t_n^{(z)})/dz \simeq -\log \Lambda$. For small n , the values for t_n and dt_n/dz deviate from the exponential scaling. The deviation is larger for smaller z , since the discretization interval at the band edge becomes narrower, i.e. is more weakly coupled to the impurity.

$$= \sum_{ij} A_{ij}^{(z)} \delta(\omega - \omega_{ij}^{(z)}), \quad (11)$$

with

$$\begin{aligned} A_{ij}^{(z)} &= |\langle E_i^{(z)} | O | E_j^{(z)} \rangle|^2 (\rho_i^{(z)} \pm \rho_j^{(z)}) \\ \omega_{ij}^{(z)} &= E_j^{(z)} - E_i^{(z)}, \end{aligned} \quad (12)$$

where O is a local operator acting at the impurity (e.g. spin, particle creation/annihilation), \pm takes $+(-)$ for a fermionic (bosonic) operator O , and $\rho_i = e^{-E_i/T} / (\sum_j e^{-E_j/T})$ is the diagonal of the density matrix at temperature T . Here we employ the full-density-matrix (fdm-) NRG^{6,14} in evaluating Eq. (11).

The dynamics of the impurity in either the SIAM or the Kondo model is described by the spin and frequency resolved \mathcal{T} -matrix for electrons scattering off the impurity. By using equations of motion¹⁵, it is given by

$$\mathcal{T}_\nu(\omega) = \begin{cases} \pi\Gamma \langle d_\nu | | d_\nu^\dagger \rangle_\omega & \text{(SIAM)} \\ \frac{\pi^2}{2D} \langle O_\nu | | O_\nu^\dagger \rangle_\omega & \text{(Kondo)} \end{cases} \quad (13a)$$

For the SIAM, this leads to the impurity spectral function $A_\nu(\omega) = -\frac{1}{\pi} \text{Im} \langle d_\nu | | d_\nu^\dagger \rangle_\omega$, whose spectral resolution can be improved by utilizing the impurity self-energy $\Sigma_\nu \equiv \langle [U n_\uparrow n_\downarrow, d_\nu] | | d_\nu^\dagger \rangle_\omega / \langle d_\nu | | d_\nu^\dagger \rangle_\omega$.¹⁶ For the Kondo model this introduces the local correlation function $\langle O_\nu | | O_\nu^\dagger \rangle_\omega$ in terms of the composite operator¹⁵ $O_\nu \equiv [f_{0\nu}, H_0^{\text{Kondo}}] = [f_{0\nu}, J \vec{S}_d \cdot \vec{S}_0]$ (see Eq. (10)).

The imaginary part of the \mathcal{T} -matrix defines the frequency and spin-resolved transmission probability

$$T_\nu(\omega) \equiv -\frac{1}{\pi} \text{Im} [\mathcal{T}_\nu(\omega)], \quad (13b)$$

which, for simplicity, will be also referred to as T -matrix (note the altered font). One has $T_\nu(\omega) \in [0, 1]$, where $T_\nu(\omega) = 1$ implies perfect transmission at given frequency ω . Furthermore, in the absence of a magnetic field, $T_\uparrow(\omega) = T_\downarrow(\omega) = T(\omega)$, with $T(\omega)$ the spin-averaged spectral data.

D. Limitations of z -averaging

Within the conventional broadening scheme,⁶⁻¹⁰ the spectral resolution can be improved by decreasing Λ and by increasing n_z , but the improvement is limited. First, for practical reasons, the choice of Λ needs to be $\gtrsim 1.7$ to ensure energy scale separation, since otherwise an excessive number of states must be kept within the NRG.¹⁷

Second, while $n_z \geq 2$ is highly attractive to gain resolution in energy space, there is no reason to expect that excessive z -averaging, i.e. $n_z \rightarrow \infty$ for finite $\Lambda \gtrsim 1.7$, can recover the exact continuum limit $\Lambda \rightarrow 1^+$. Moreover, there turns out to be a practical limit in z -averaging, typically $n_z \lesssim 64$ [10], since there exist unavoidable slight inequivalences of the spectral data of different z -shifts. While the coefficients t_n in Eq. (9) scale as $\sim \Lambda^{-n/2-z}$ for large n , z -dependent variations of $t_n \Lambda^{n/2+z}$ occur for smaller n as seen in Fig. 1(a). These originate from the disruption of the logarithmic scaling at the band edge: for example, if one strictly adheres to the discretization $\pm \Lambda^{-k+1-z}$ ($k = 1, 2, \dots$) near the band edge, a narrow discretization interval emerges at the band edge for $z \ll 1$. The corresponding coarse-grained level possesses a *large* level energy since it resides at the band edge, yet is *weakly* coupled to the impurity. As a consequence, $z \rightarrow 0^+$ compromises energy scale separation. This manifests itself in a peak-like structure in the scaled hopping amplitudes $t_n \Lambda^{n/2+z}$ in Fig. 1(a) that shifts towards smaller energies, i.e. larger n as z is reduced.¹⁸ Therefore the iterative NRG diagonalization along the Wilson chain intrinsically faces increasing difficulty with $z \rightarrow 0^+$. The resulting bias with respect to different z translates into slightly uneven distribution of spectral weights after z -averaging. Though the unevenness is smoothed by large enough broadening for small n_z , it introduces “noise” for larger n_z (e.g. see dash-dot line in Fig. 3(a)). Hence the gain in spectral resolution slows down with increasing n_z .

III. BROADENING DISCRETE DATA

In order to recover the continuum from the discrete spectral data A_z^{disc} in Eq. (11), we first need to gather the discrete spectral data in a suitable way. Since we

will associate each discrete weight not only with an individual energy ω_{ij} but also with an individual broadening width σ_{ij} [specified in Eq. (19) below], we will use a *two-dimensional* binning scheme (instead of the usual one-dimensional scheme used when all weights are broadened by the same width). For this, we introduce a fine-grained binning in log-frequency space (about 250 to 500 bins per decade) as well as a linear binning in the broadening width σ (e.g. linearly spaced between $[0.01, \sigma_{\max}]$ with spacing 0.01, where σ_{\max} can be chosen differently in different contexts; $\sigma_{\max} = 2 \log \Lambda$ is enough at $T = 0$, while $\sigma_{\max} = 8 \log \Lambda$ was used for finite T for the sake of the analysis). A discrete spectral weight A_{ij} at ω_{ij} and broadening σ_{ij} can then be associated with bin k at frequency ω_k and broadening σ_k , i.e. it is added to a two-dimensional array

$$A_{ij}^{(z)} \text{ at } (\omega_{ij}, \sigma_{ij})_z \rightarrow A_z(\omega_k, \sigma_k). \quad (14)$$

While the first dimension (binning in ω) is standard within the NRG,² the binning in an adaptive σ is new. Subsequent z -averaging then is easily performed on the level of the fine-grained binned data array in $A(\omega_k, \sigma_k)$,

$$\bar{A} \equiv \langle A \rangle_z = \frac{1}{n_z} \sum_z A_z \quad (15)$$

The broadening scheme proposed in this paper is based on using the above z -averaged two-dimensional array \bar{A} as input for the following broadening formula:

$$A(\omega) = L_\gamma \left[\sum_k \bar{A}(\omega_k, \sigma_k) \delta_{\bar{\sigma}_k}(\omega; \omega_k) \right]. \quad (16)$$

Here the broadening consists of two subsequent steps: First the discrete spectral data in bin $\bar{A}(\omega_k, \sigma_k)$ is broadened using a standard NRG log-Gaussian broadening kernel^{2,6} $\delta_{\bar{\sigma}_k}(\omega; \omega_k)$ [see Eq. (17a) below], centered around ω_k , yet with individual broadening width $\bar{\sigma}_k \equiv \frac{\alpha}{n_z} \sigma_k$, where α is an overall constant prefactor [see Eq. (17b) below]. This first step is applied to the spectral data at *all* frequencies, yet it only generates smooth data for frequencies $\omega > T$. It still leaves pronounced discrete features for $|\omega| \lesssim T$.

In a second step we employ uniform linear broadening $L_\gamma[\cdot]$ of optimized width $\gamma \lesssim T$ [cf. Eq. (21) below]. The latter is again applied to the full frequency range, thus there is no need to specify a transition function for switching from log-Gaussian to linear broadening (in contrast to the conventional scheme of Ref. 6). Consequently, while there is minor numerical overhead involved by considering the full frequency range, the latter minimizes artefacts in the final spectral data for intermediate frequencies $|\omega| \sim \gamma$. For exponentially large frequencies $|\omega| \gg T \gtrsim \gamma$, where the data obtained from the first log-Gaussian broadening step is already smooth, the uniform broadening $L_\gamma[\cdot]$ has negligible effect, so eventually may be skipped there.

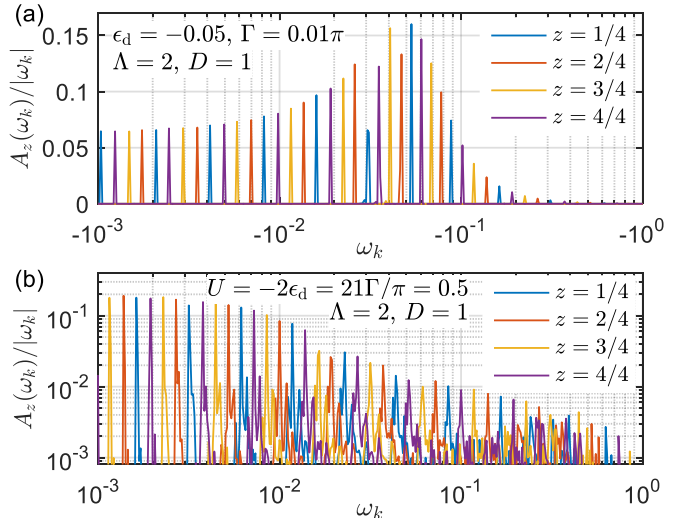


FIG. 2. Discrete spectral data $A_z(\omega_k) \equiv \sum_{\sigma_k} A_z(\omega_k, \sigma_k)$ for (a) the non-interacting resonant level model [see Eq. (22)] and (b) the SIAM at $T = 0$. Different colors denote different z -shifts. Since the bin k at frequency ω_k has width proportional to $|\omega_k|$ in the frequency domain, $A_z(\omega_k)/|\omega_k|$ is related with the height of a subsequently broadened curve. The discrete spectral weights are bunched, and most of bunches are uniformly spaced in log-frequency space with the spacing $\Delta(\log |\omega|) \simeq (\log \Lambda)/n_z$ after z -averaging. But in certain regimes [$\omega_k \sim \epsilon_d = -0.05$ for (a) and $\omega_k \sim U/2 = 0.25$, $\omega_k \sim T_K \simeq 0.01$ for (b)], bunches are widely spread or irregularly distributed: the adaptive broadening scheme systematically applies the narrower broadening width to these bunches, leading to the improved spectral resolution in such regimes (see Fig. 3 and 5). See Secs. IV A and IV B for detail.

Another approach to improve the spectral resolution¹⁹ first converts the discrete data to the imaginary-frequency domain via the Hilbert transform and then applies the analytic continuation to obtain real-frequency curves (without imposing broadening). However, the analytic continuation is numerically ill-posed and thus subject to error. Indeed, as the impurity solver of the DMFT, the NRG is advantageous exactly for the reason that the dynamical properties are directly computed on the real-frequency axis without the analytic continuation.⁵

In the following, we discuss the individual steps above in more detail. For simplicity, we start with the conventional and adaptive broadening schemes for the regime $|\omega| > T$, in which all the weights are logarithmically distributed. Then we address the regime $|\omega| \lesssim T$. For all of the following discussion we already assume z -averaged discrete NRG data, unless indicated otherwise.

A. Broadening for $|\omega| > T$

The discrete spectral contributions of $A_z^{\text{disc}}(\omega)$ are bunched in log-frequency space, where average distance between bunches $\Delta(\log |\omega|) \simeq (\log \Lambda)/n_z$ after z -

averaging, as illustrated in Fig. 2. This originates from the underlying discretization grid: due to the logarithmic discretization, the discretized energy levels of the bath are located at $\sim \pm \Lambda^{-k+1-z}$ ($k = 1, 2, \dots$), that is, uniformly spaced in log-frequency space (except near the band edges). By coupling the impurity to the bath, the energy levels of the total system are shifted from the bare bath energy levels, but the overall logarithmic distribution remains.

We use the standard NRG log-Gaussian broadening kernel^{2,6}

$$\delta_{\bar{\sigma}_k}(\omega; \omega_k) = \frac{\Theta(\omega\omega_k)}{\sqrt{\pi}\bar{\sigma}_k|\omega_k|} e^{-\left(\frac{\log|\omega/\omega_k| - \frac{\sigma_k}{4}}{\bar{\sigma}_k}\right)^2}, \quad (17a)$$

which preserves the spectral sum rule and Kondo peak height,⁶ yet where we explicitly introduce an individually determined broadening width

$$\bar{\sigma}_k \equiv \underbrace{\frac{\alpha}{n_z}}_{\equiv \alpha_z} \sigma_k \quad (17b)$$

with α an overall constant prefactor of order 1. In this work, we choose $\alpha \in [1, 2]$ and specify its value with each figure below. We use $\alpha = 1$ for the non-interacting resonant level model, $\alpha \in \{1.5, 2\}$ for the SIAM and Kondo model at $\Lambda = 2$, and $\alpha = 2$ also for extremely large $\Lambda \lesssim 16$ [cf. Fig. 10]. The bar on the l.h.s. of Eq. (17b) is a reminder that this is the final broadening used on the z -averaged data as in Eq. (15).

Conventional broadening schemes^{6,7} use a constant $\sigma_k = \log \Lambda$ for all discrete spectral weights (i.e. $\bar{\sigma}_k = \text{const} \lesssim \log \Lambda$). This choice is natural for the discrete weights deep inside fixed-point regimes such as the stable low-energy fixed-point where the spectral data is featureless and the spectral data appears bunched at distance $\Delta(\log|\omega|) = (\log \Lambda)/n_z$ in log-frequency space, suggesting $\alpha = 1$. However, this leads to overbroadening of sharp spectral features at finite frequencies $|\omega| \gtrsim T$ where discrete weights are distributed more irregularly in relation to the underlying physics.

1. Adaptive broadening σ_k

The broadening scheme proposed in this paper uses the log-Gaussian in Eq. (17a) with the adaptive broadening width in Eq. (17b) where

$$\sigma_{ij} \xrightarrow{\text{binning}} \sigma_k. \quad (18)$$

Here σ_{ij} is determined for each spectral weight A_{ij} at frequency ω_{ij} for an arbitrary but fixed z -shift as in Eq. (11), and then binned according to Eq. (14). In the following we describe and motivate a scheme for computing σ_{ij} for an elementary spectral contribution A_{ij} prior to z -averaging.

For the sake of the argument, suppose the discrete data $A_z^{\text{disc}}(\omega)$ can be obtained exactly by solving $H(z)$

in Eq. (7) without any truncation. As the coefficients in $H(z)$ are continuous functions of z , the frequency $\omega_{ij}^{(z)}$ associated with each discrete spectral weight $A_{ij}^{(z)}$ shifts as a function of z . In particular, a shift $z \rightarrow z + 1$ shifts the discrete data onto itself (except for the very band edge). Now to fill the distance between a delta-peak of weight $A_{ij}^{(z)}$ at frequency $\omega_{ij}^{(z)}$ and another delta-peak of weight $A_{ij}^{(z+\Delta z)}$ at $\omega_{ij}^{(z+\Delta z)}$, with $\Delta z \equiv 1/n_z \ll 1$, a sensible choice for the broadening width σ_{ij} for $A_{ij}^{(z)}$ is to use the resulting shift in log-frequency scale, $|\log|\omega_{ij}^{(z)}| - \log|\omega_{ij}^{(z+\Delta z)}||$, up to a factor σ_0 of order 1. To leading order we thus choose

$$\sigma_{ij}^{(z)} \equiv \left| \frac{d \log|\omega_{ij}^{(z)}|}{dz} \right| = \frac{1}{|\omega_{ij}^{(z)}|} \left| \frac{dE_j}{dz} - \frac{dE_i}{dz} \right| \quad (19a)$$

$$= \frac{1}{|\omega_{ij}^{(z)}|} \left| \langle E_j | \frac{dH}{dz} | E_j \rangle - \langle E_i | \frac{dH}{dz} | E_i \rangle \right|, \quad (19b)$$

where the last expression is evaluated within an NRG run at fixed z -shift. Here we used the Hellmann-Feynmann theorem $\frac{dE_i}{dz} = \langle E_i | \frac{dH}{dz} | E_i \rangle$, given that the NRG is dealing with (approximate) eigenstates $|E\rangle_i$ of the Hamiltonian H (for further details, see App. B). Therefore overall the adaptive broadening $\sigma_{ij}^{(z)}$ is computed as the lowest-order response to the perturbation $\frac{dH}{dz}$. [Actually, the full perturbation is $\frac{dH}{dz} \cdot \Delta z$; the factor $\Delta z = 1/n_z$, however, has already been split off in Eq. (17b); hence $\frac{dH}{dz}$ will be referred to as the perturbation here.]

Finally, the perturbation $\frac{dH}{dz}$ in Eq. (19) for the Wilson chain for a given z -shift is obtained numerically as follows: the standard Lanczos tridiagonalization of the bath is performed for two closeby shifts z and $z + \delta z$, with e.g. $\delta z = 0.01/n_z \ll \Delta z$. This gives two Wilson chains with slightly altered coefficients t_n . The perturbation $\frac{dH}{dz}$ is therefore defined in the same geometry as the Wilson chain, but with different hopping amplitudes

$$\frac{dt_n}{dz} \simeq \frac{1}{\delta z} (t_n^{(z+\delta z)} - t_n^{(z)}), \quad (20)$$

instead of t_n . A typical set of the coefficients dt_n/dz of the perturbation dH/dz is presented in Fig. 1(b). For simplicity, we use the particle-hole symmetric hybridization $\Gamma(\epsilon) = \Gamma(-\epsilon)$ throughout this work. Hence the onsite energy for each Wilson site is zero by symmetry and thus trivially independent of z -shifts. For general $\Gamma(\epsilon)$, nevertheless, the onsite energies can be simply incorporated within the tridiagonalization, with the numerical derivatives of the resulting onsite energies along the Wilson chain computed analogously to Eq. (20). See also App. A for further details.

Note that the two Lanczos tridiagonalizations for slightly different z -shifts above effectively address a *different* one-particle basis $f_{n\nu}$ [cf. Eq. (9)] via a slightly shifted coarse-graining of the bath. However, this leads to two Wilson chains of identical structure, differing only in their parameters. Hence without restricting the above argument, the operators $f_{n\nu}$ may be considered independent of z -shifts, and the only changes in the bath are

described by the coefficients $t_n^{(z)}$. With this, the diagonal matrix elements of the perturbation, $\langle E_i | \frac{dH}{dz} | E_i \rangle$ in Eq. (19), can be straightforwardly evaluated directly during the iterative diagonalization of NRG.

B. Broadening for $|\omega| \lesssim T$

Finite temperature T introduces an energy scale where energy scale separation necessarily comes to a halt. Even if the Wilson chain itself is semi-infinite, finite T introduces an effective finite length of the chain $n_T \sim -2 \log_\Lambda T$ within fdm-NRG.^{6,14} This intrinsically limits the energy resolution to the order of T . Consequently, the log-Gaussian broadening must eventually be replaced by a linear broadening scheme for $|\omega| \ll T$. This also ensures that the spectral data for positive and negative frequencies is smoothly connected across $\omega = 0$. In practice, this is achieved by using various linear broadening kernels, such as Gaussians⁶ or Lorentzians⁷ of width $\gamma \lesssim T$ in linear frequency.

However, the transition from the log-Gaussian to linear broadening involves some arbitrariness, and tends to introduce artificial features at intermediate frequencies at $|\omega| \sim T$. While these artefacts can be reduced to some extent by carefully combining two kernels⁶, it is difficult to have a generic scheme to avoid artefacts for a general parameter regime where pronounced spectral features occur on the scale of temperature. This is specifically relevant for DMFT type calculations.^{2-5,7}

In many cases, discretization artefacts can be systematically suppressed at all frequencies, including both $|\omega| \lesssim T$ as well as $|\omega| \gg T$, by exploiting self-energy improved spectral functions,¹⁶ to be referred to as “ Σ -improved” in the analysis below. However, as this self-energy “trick” is the post-processing of smoothed spectral data, the main focus here is to find an optimal way of *directly* broadening discrete spectral data before any post-processing.

The essential observation here is that we would like to avoid altogether a transition function from one broadening kernel to another, i.e. log-Gaussian to linear broadening. To achieve this, we perform the log-Gaussian broadening for *all* frequencies, followed by a linear broadening that again also operates on *all* frequencies, i.e. we use a convolution of two broadening kernels as in Eq. (16). This scheme thus avoids constructing an ad-hoc scheme for transitioning from one type of broadening to another.

The order in which the broadening kernels are applied is important. Since the log-Gaussian broadening does not affect the function at $\omega = 0$, by construction, the value of T -matrix at $\omega = 0$ is determined at the stage of the linear broadening. If one applies the linear broadening first, the value $T(0)$ is determined directly from discrete data, so is subject to numerical noises. On the other hand, if the log-Gaussian broadening is applied first, the linear broadening acts on the curve which is already smooth for $|\omega| \gtrsim T$ in log-frequency space [see blue line in Fig. 11(a)], so re-

sults in smooth curves across $\omega = 0$. Solid and dashed lines in Fig. 11(c,d) illustrates the results from the “correct” and opposite orders, respectively: with the opposite broadening order, the value $T(0)$ is clearly shifted from the correct value $\simeq 1$ and the fitting error ε_{RMS} is much larger (see Sec. V 2 for detail).

For the linear broadening using the convolution $L_\gamma[g] = \int d\omega' \delta_\gamma(\omega - \omega') g(\omega')$ in Eq. (16), we choose the derivative of the Fermi-Dirac distribution function $f(\omega)$,

$$\begin{aligned} \delta_\gamma(\omega - \omega') &\equiv -\frac{d}{d\omega} f(\omega - \omega') \\ &= \frac{1}{2\gamma} \left(1 + \cosh \frac{\omega - \omega'}{\gamma} \right)^{-1}, \end{aligned} \quad (21)$$

at an effectively reduced “temperature” $\gamma < T$. This kernel decays more slowly for large frequencies than a regular Gaussian. Hence it promises somewhat smoother data, whereas it still decays exponentially, in contrast to Lorentzians⁷. Last but not least, the above choice is also motivated by the empirical fact that the linear conductance, which exactly corresponds to a spectral function convolved with $-df/d\omega|_{\gamma=T}$ at $\omega = 0$, can be very accurately computed within the NRG by convolving the *discrete* spectral data of the NRG with $-df/d\omega$.⁶

It remains to find the optimal value for the linear broadening width γ . It should be chosen such that (i) it removes the residual discrete features from the prior log-Gaussian broadening for frequencies $|\omega| \lesssim T$, yet (ii) that it minimally overbroadens the remaining data otherwise. Large γ guarantees smooth data as argued above, which in practice means that $\gamma = T$ is more than sufficient to obtain smooth data. Minimizing $0 < \gamma < T$ in a systematic fashion while maintaining smooth data to within about 0.2% variations will be addressed in Sec. V below.

IV. RESULTS AT $T = 0$

In this Section, we compute the T -matrix in Eq. (13) for non-interacting and interacting impurity models at $T = 0$, and demonstrate that the adaptive broadening scheme provides overall better spectral resolution than the conventional scheme.

A. Noninteracting resonant level model

We apply the adaptive broadening scheme to the non-interacting resonant level model of spinless fermions,

$$H = \epsilon_d d^\dagger d + \int_{-D}^{+D} d\epsilon \left(\sqrt{\frac{\Gamma}{\pi}} (d^\dagger c_\epsilon + c_\epsilon^\dagger d) + \epsilon c_\epsilon^\dagger c_\epsilon \right), \quad (22)$$

which is the spinless one-band SIAM with $U = 0$. Since the Hamiltonian is quadratic, the T -matrix for particles scattering off the impurity $T(\omega) = \pi \Gamma A(\omega) =$

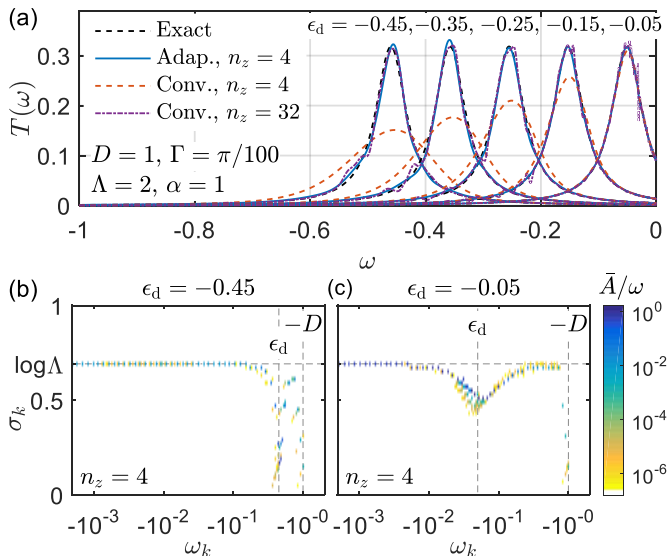


FIG. 3. Adaptive broadening for the T -matrix in the spinless non-interacting resonant level model. Panel (a) shows the exact $T(\omega)$ [Eq. (23), black dashed line] and the NRG results with the conventional and adaptive broadening schemes for different ϵ_d . For small n_z , the conventional scheme (strongly) overbroadens the resonance peaks (red dashed line), while the adaptive scheme (blue solid line) nicely reproduces the exact $T(\omega)$. In contrast, the conventional broadening scheme can capture the sharp peak shapes only for much larger n_z (purple dash-dot line), but also acquires noise [cf. Sec. IID]. Panels (b) and (c) show the binned discrete data $\bar{A}(\omega_k, \sigma_k)/|\omega_k|$ (\bar{A}/ω for short; see text) for $\epsilon_d = -0.45$ and $\epsilon_d = -0.05$, respectively. The weights near $\omega_k \simeq \epsilon_d$ as well as near the band edge $-D$ have clearly reduced adaptive broadening width $\sigma_k < \log \Lambda$. Thus the adaptive broadening can capture the sharp features near $\omega_k \simeq \epsilon_d$ and band edges $|\omega_k| = D$ (not shown in (a)) much better than the conventional broadening scheme for fixed n_z .

$-\Gamma \text{Im}\langle d||d^\dagger \rangle_\omega$ has the closed form

$$T(\omega) = \frac{\Gamma^2 \Theta(D - |\omega|)}{\left(\omega - \epsilon_d - \frac{\Gamma}{\pi} \log \left| \frac{D+\omega}{D-\omega} \right| \right)^2 + \Gamma^2}, \quad (23)$$

with $D = 1$ as usual. When $\Gamma, |\epsilon_d| \ll 1$, $T(\omega)$ approximates a Lorentzian centered at ϵ_d of width 2Γ . For the simulation of this model using NRG, we kept up to 200 states in each step of iterative diagonalization.

Though the model is quadratic and simple, the NRG with the conventional broadening is very inefficient in reproducing $T(\omega)$ in Eq. (23) when the resonance is sharp in the sense $\Gamma \ll |\epsilon_d|$. Since every discrete weight is broadened with the fixed width-to-position ratio, the resonance in $T(\omega)$ cannot be narrower than $|\epsilon_d| \cdot \frac{\alpha}{n_z} \log \Lambda$. As seen in Fig. 3(a), this makes the peaks overbroadened when $\Gamma/|\epsilon_d| \ll \log \Lambda/n_z$ as compared to the exact $T(\omega)$ [cf. Eq. (23)]. Also, Fig. 3(a) shows that excessive z -averaging with $n_z = 32$ does not only sharpen the resonance peak but also introduces noise as discussed in Sec. IID. In contrast, the adaptive broadening already

captures the resonance peaks at much lower z -averaging ($n_z = 4$). This can be understood by analyzing the distribution of discrete binned spectral weights $\bar{A}(\omega_k, \sigma_k)$ which are z -averaged as in Eq. (15).

Figure 3(b,c) presents a snapshot of the adaptively determined broadening by directly plotting the binned data $\bar{A}(\omega_k, \sigma_k)/|\omega_k|$, which is related with the height of a subsequently broadened curve as mentioned in Fig. 2. Hence for the purpose of analysis of the discrete data later in this paper, we show the array $\bar{A}(\omega_k, \sigma_k)/|\omega_k|$ (\bar{A}/ω in short). In Fig. 3(b,c) then, three features can be distinguished in the distribution of \bar{A}/ω : (i) For $|\omega_k - \epsilon_d| \gg \Gamma$, the weights are concentrated along the line $\sigma_k \simeq \log \Lambda$. These weights, including the stable low-energy fixed point regime, are almost uniformly distributed in equally spaced bunches in log frequency. Consequently, the adaptive broadening assigns the same broadening width as the conventional one; $\bar{\sigma}_k = \frac{\alpha}{n_z} \log \Lambda$. (ii) At the maximum of $T(\omega)$ around $\omega_k \simeq \epsilon_d$, the weights in \bar{A}/ω show a clearly reduced broadening width σ_k that can be much narrower than in the conventional scheme [e.g. see panel (b)]. This is important in order to capture the sharp peak structure. (iii) Near the band edges $|\omega_k| \simeq D = 1$, similar to (ii), again the weights have clearly reduced $\sigma_k < \log \Lambda$. Here they describe the sharp edges of $A(\omega)$ at $\omega = \pm D$ in Eq. (23), which originates from the sharp edge of the hybridization function $\Gamma(\epsilon)$.

B. Kondo and SIAM at $B = 0$

In this Section and the next, we analyze the dynamical behavior of the Kondo model and the SIAM over a wide range of magnetic field B , starting with the case $B = 0$. Here the frequency resolved T -matrix [cf. Eq. (13)] shows the well-known Kondo resonance at $\omega = 0$ as seen in Figs. 4 and 5 for the Kondo model and the SIAM, respectively. The height of the Kondo peak is determined by Friedel sum rule. The NRG gives $T(\omega = 0) \simeq 1$ accurately to within 1% error in either model. When also self-energy is exploited for improved spectra data in the SIAM, the error further decreases. The width of the Kondo peak is the Kondo temperature T_K , up to an $O(1)$ factor depending on the precise definition. For both Kondo and Anderson models, we determined T_K as the frequency ω at which the dynamical impurity spin susceptibility $\chi_s(\omega) \equiv -\frac{1}{3\pi} \text{Im}\langle \vec{S}_d || \vec{S}_d \rangle_\omega$ becomes maximum²⁰ (here the factor $1/3$ comes from the average of the components in $\vec{S}_d \cdot \vec{S}_d$ when exploiting SU(2) spin symmetry, e.g. see Ref. 21). In the simulations, we kept up to 500 multiplets in each step of the iterative diagonalization when exploiting SU(2)_{spin} \otimes SU(2)_{ph} for spin and particle-hole symmetry, respectively.

Both the Kondo as well as the SIAM share the same Kondo physics around $|\omega| \lesssim T_K$, as well as the sharp cutoff outside the band edge $|\omega| > D$. The Hubbard side peaks of the SIAM, however, are absent in the Kondo model. The adaptive broadening enhances the resolu-

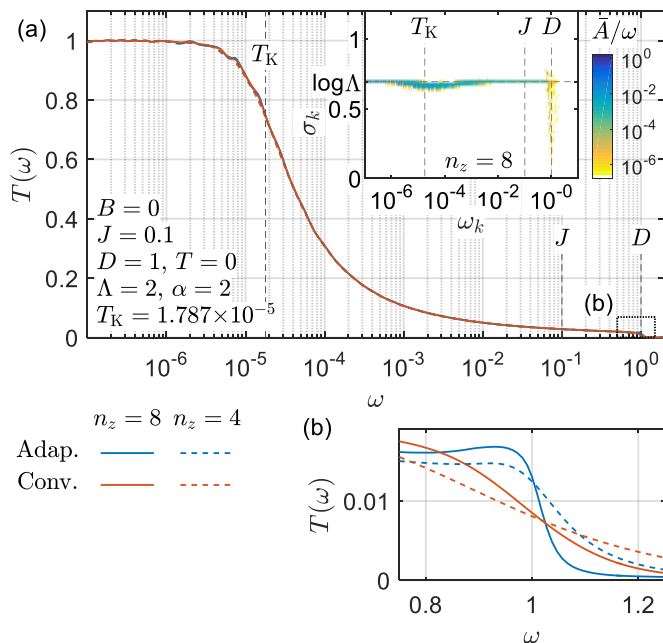


FIG. 4. T -matrix of the Kondo model for $B = T = 0$. Due to total spin and particle-hole symmetries, $T_\nu(\pm\omega) = T(\omega)$. (a) Broadened curves with different broadening schemes (adaptive or conventional) and number of z -shifts ($n_z = 4$ and 8). (Inset) Discrete spectral data \bar{A}/ω for the data in the main panel. (b) Close-up near the band edge $D = 1$. The adaptive broadening better resolves the sharp edge at $|\omega| = D$, which stems from the reduced broadening $\sigma_k < \log \Lambda$ at $|\omega_k| \simeq D$ in the inset of (a).

tion of the high-frequency features, as in Fig. 4(b) and Fig. 5(c). Quite generally, the enhancement is more significant where features are overbroadened in the conventional scheme. In particular, this is the case when n_z is smaller, Λ is larger, and in case of the SIAM, no self-energy is used. In Sec. IV D, we further discuss the performance of adaptive broadening for large Λ . Here in the insets of Fig. 4(a) and Fig. 5(a), we show for fixed $\Lambda = 2$ where and how the adaptive broadening of the discrete spectral data \bar{A}/ω enhances the resolution. The broadening is clearly reduced at the band edges $|\omega_k| = D$, and for the SIAM also around the Hubbard side peaks, $|\omega_k| \simeq U/2$, in that the distribution in σ_k clearly spreads to lower values. Also, for the SIAM, the spread in σ_k at $|\omega_k| = D$ is much less pronounced, since at $|\omega_k| \gg U/2$ the spectral weight decays more strongly as compared to the Kondo model.

The adaptive broadening gives quantitatively the same Kondo peak shape as the conventional broadening, since it is located around $\omega = 0$ where the resolution is exponentially refined due to the underlying logarithmic discretization. Furthermore, given the relatively slow logarithmic corrections that enter the Kondo peak shape, the discrete weights \bar{A}/ω for $|\omega_k| \lesssim T_K$ are mostly distributed around $\sigma_k \simeq \log \Lambda$.

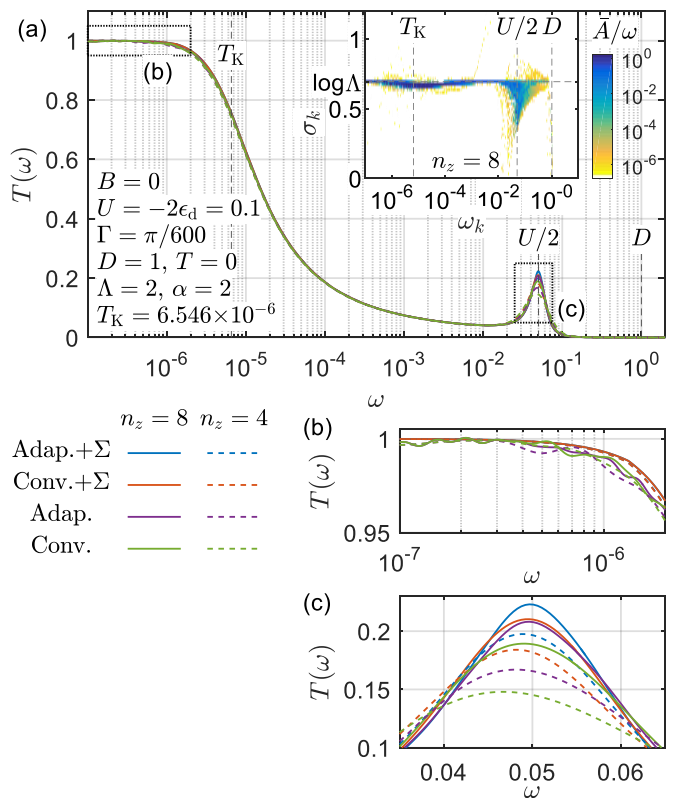


FIG. 5. T -matrix of the SIAM for $B = T = 0$. Due to total spin and particle-hole symmetries, $T_\nu(\pm\omega) = T(\omega)$. (a) Broadened curves with different broadening schemes (adaptive or conventional), number of z -shifts ($n_z = 4$ and 8), and partly improved by self-energy (Σ). (b) Close-up of the Kondo peak at $\omega \ll T_K$, showing convergence to within 1%. Here the blue solid (dashed) line coincides with the red solid (dashed) line. (c) Close-up of the Hubbard side peak centered at $\omega = U + \epsilon_d = U/2$. The self-energy removes discretization related noise at $\omega \ll T_K$ and sharpens the Hubbard side peaks. The inset to panel (a) presents the discrete spectral data \bar{A}/ω for the data in the main panel. It shows that the adaptive broadening reduces the broadening σ_k for frequencies $\omega_k \simeq U/2$, and hence enhances the resolution of the side peak. This is more significant for smaller n_z or without self-energy.

C. Kondo and SIAM at large B

Next we apply a large magnetic field $B \gg T_K$, which splits the Kondo peak of $T(\omega) = \frac{1}{2} \sum_{\nu=\uparrow,\downarrow} T_\nu(\omega)$ in between the different spins ν . The split Kondo peaks are located at $\omega = \pm(B - \Delta\omega_B)$ for $\nu = \uparrow$ and $\nu = \downarrow$, respectively. The shift $\Delta\omega_B \simeq -B/[2 \log(B/T_K)]$ is suggested by analytic RG calculations^{23,24} and numerically confirmed by density-matrix renormalization group results²². Here by having $B \neq 0$, the symmetry $SU(2)_{\text{spin}} \otimes SU(2)_{\text{ph}}$ above is reduced to $U(1)_{\text{spin}} \otimes SU(2)_{\text{ph}}$, where we kept up to 2,000 multiplets in each step of iterative diagonalization.

As illustrated in Figs. 6 and 7, the adaptive broaden-

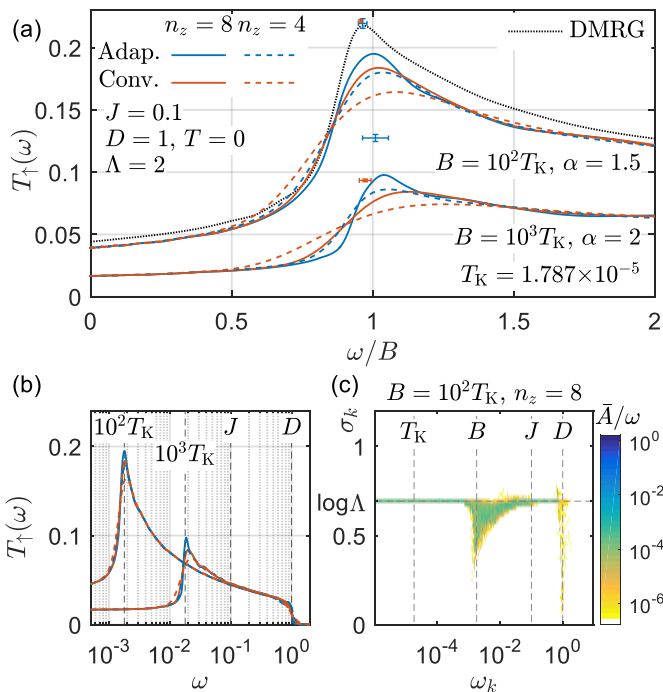


FIG. 6. T -matrix of the Kondo model for large magnetic field $B \gg T_K$ at $T = 0$. Due to particle-hole symmetry, $T_\uparrow(\omega) = T_\downarrow(-\omega)$. (a,b) Broadened curves at $B/T_K = 10^2$ and 10^3 , plotted versus (a) ω/B and (b) ω , with different broadening schemes (adaptive or conventional) and number of z -shifts ($n_z = 4$ and 8). The blue and red crosshairs in (a) indicate the value and uncertainty for the peak positions and heights extrapolated to the limit $\alpha_z \rightarrow 0$ for adaptive and conventional schemes, respectively, as derived from Fig. 8. The extrapolated peak position at $B = 10^2 T_K$ is consistent with the DMRG result (dotted line, taken from Ref. 22). (c) Discrete spectral data \bar{A}/ω for the data in panel (a) for the parameters as indicated.

ing systematically improves the resolution of the Kondo peaks for $B \gg T_K$, in addition to the sharp edge at $|\omega| = D$ in the Kondo model and the Hubbard side peak at $|\omega| = U/2$ in the SIAM. Overall we observe that for a fixed ratio of $B/T_K \gg 1$, the position ω_{\max} of the Kondo peak is slightly larger in the Kondo model (see also Figs. 8 and 9 below). The overall line shape of the curves are similar otherwise. As B increases, the peak line shapes remain qualitatively similar as a function of ω/B , except that the peak position slightly shifts towards $\omega/B = 1$ and that the peak height is reduced. Eventually, for the SIAM when $B \gtrsim U/2$, the Kondo peak merges with the Hubbard side peak.

For the SIAM as well as the Kondo model, we choose a slightly larger $\alpha = 2$ for $B = 10^3 T_K$ than $\alpha = 1.5$ for $B = 10^2 T_K$ to smear out the residual noise from z -averaging at $n_z = 8$ [cf. Sec. IID]. This noise persists even if we adjust the width of the outmost discretization interval in different ways as a function of z , or if we increase the number of kept states. Overall we again observe that the

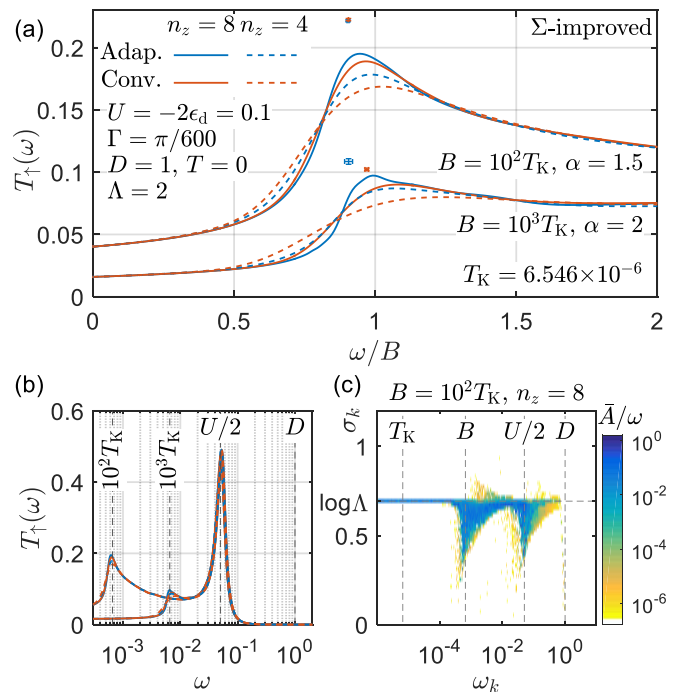


FIG. 7. T -matrix of the Anderson model for large magnetic field $B \gg T_K$ at $T = 0$. Due to particle-hole symmetry, $T_\uparrow(\omega) = T_\downarrow(-\omega)$. (a,b) Broadened curves at $B/T_K = 10^2$ and 10^3 , versus (a) ω/B and (b) ω , with different broadening schemes (adaptive or conventional) and number of z -shifts ($n_z = 4$ and 8). All curves are improved by utilizing the self-energy Σ . The blue and red crosshairs in (a) indicate value and uncertainty of the peak positions and heights extrapolated to the limit $\alpha_z \rightarrow 0$ for adaptive and conventional schemes, respectively, as extracted from Fig. 9. (c) Discrete spectral data \bar{A}/ω for the data in panel (a) for the parameters as indicated.

adaptive broadening leads to improved performance.

We estimate the height T_{\max} and the position ω_{\max} of the Kondo peaks in the continuum limit, by extrapolating their values at finite broadening $\bar{\sigma}_k \propto \alpha_z \equiv \alpha/n_z$ to $\alpha_z \rightarrow 0$. In Fig. 8(c,d) and Fig. 9(c,d), we plot the heights T_{\max} and positions ω_{\max} of the peak vs. α_z obtained from different choices of n_z and α . For both, adaptive as well as conventional broadening, T_{\max} and ω_{\max} show consistent dependency solely on the ratio α_z . In detail, the consistency is somewhat better within the conventional approach (since uniformly overbroadened), whereas minor offsets between different n_z values can be observed in the adaptive broadening.

For the extrapolation $\alpha_z \rightarrow 0$ we introduce lower and the upper cutoffs α_z^{\min} and α_z^{\max} , respectively, for the range of α_z to be included in the extrapolation. Here α_z^{\min} is required to avoid resolving the underlying discrete frequencies due to finite Λ and n_z [see the insets of Figs. 8(d) and 9(d)]. Very large α_z , on the other hand, leads to excessive overbroadening such that peak height and position become dependent on the line shape of the spectral data over a wider region, thus invalidating simple

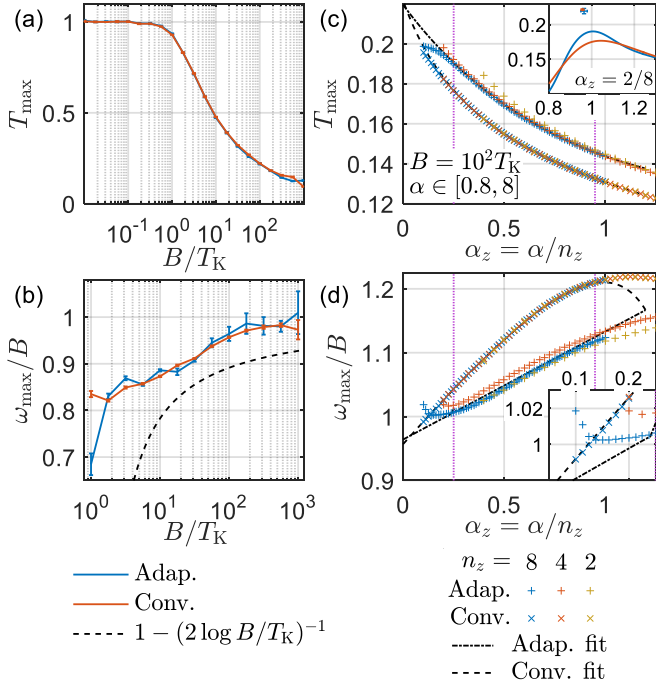


FIG. 8. Extrapolation of the Kondo peak in $T_{\uparrow}(\omega)$ for the Kondo model towards the “continuum limit” $\alpha_z \equiv \alpha/n_z \rightarrow 0$, in terms of (a) heights T_{\max} and (b) positions ω_{\max} vs. B/T_K . For ω_{\max} , we compare with the analytic prediction (dashed line). At $B = 100 T_K$, we show (c) T_{\max} and (d) ω_{\max} vs. α_z (see Fig. 6 for remaining parameters). For each magnetic field, we extrapolate T_{\max} and ω_{\max} to $\alpha_z \rightarrow 0$ by fitting the data points from $n_z = 4, 8$ within the fitting range $[0.25, 0.95]$ as indicated by the vertical dotted lines with a Padé approximant of order $[2/1]$ (dashed and dash-dot lines). The inset in (c) shows the adaptively (blue) and the conventionally (red) broadened curves of $T_{\uparrow}(\omega)$ at $B = 100 T_K$, $\alpha = 2$ and $n_z = 8$, where $\alpha_z = 0.25$ is on the lower edge of the fitting range. The extrapolated peak positions and heights are depicted as crosshairs. The inset in (d) shows a close-up of the data points and the fitted curves of ω_{\max}/B vs. α_z at small α_z . The upturn of ω_{\max} for the smallest α_z appears with the onset of underbroadening.

lower-order polynomial fits. For example, in Figs. 8(d) and 9(d) we observe a qualitative change in the extracted peak position ω_{\max} for $\alpha_z \gtrsim 1$ which we attribute to excessive overbroadening. For the results in this Section, we use the fitting range $\alpha_z \in [0.25, 0.95]$ for the Kondo model and $\alpha_z \in [0.2, 0.9]$ for the SIAM. For the fitting, we use a Padé approximant of order $[2/1]$, i.e. the ratio of a quadratic over a linear polynomial. We estimate the error bar for the extrapolated value for $\alpha_z \rightarrow 0$ as the 95% confidence interval out of this fit.

The extrapolated values T_{\max} and ω_{\max} vs. B/T_K are presented in Fig. 8(a,b) for the Kondo model and Fig. 9(a,b) for the Anderson model. T_{\max} shows a crossover around $B \sim T_K$, which smoothly connects the value at $B = 0$ (e.g. see Figs. 4 and 5) to the regime of large B (e.g. see Figs. 6 and 7). We also compare our

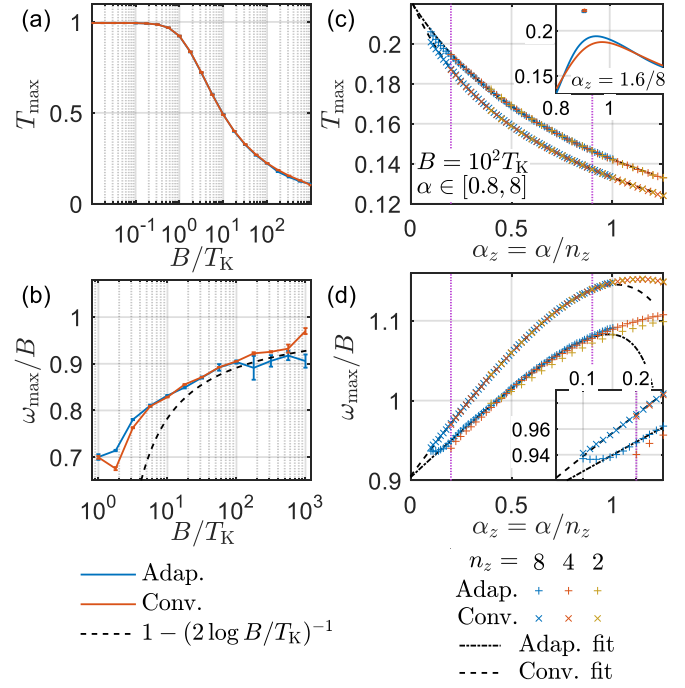


FIG. 9. Same as Fig. 8, but for the SIAM. The fitting range in (c,d) is $\alpha_z \in [0.2, 0.9]$.

NRG result of ω_{\max}/B with the analytic prediction^{23,24} $1 - \Delta\omega_B/B = 1 - (2 \log B/T_K)^{-1}$ [black dashed lines in Figs. 8(b) and 9(b)]. While the extrapolated ω_{\max}/B for the Kondo model systematically deviates from this analytical prediction, the one for the SIAM traces the analytical prediction more closely. Besides that for the SIAM we exploit self-energy to get improved spectral data, the difference with the Kondo model may also result from the fact that the Kondo model is affected by finite bandwidth D whereas by having $U \ll D$ the SIAM is not (e.g. see Ref. 20).

Overall, for both models the adaptive broadening clearly gives consistently better peak resolution in terms of T_{\max} and ω_{\max} for any finite α_z , as compared to the conventional broadening [see Figs. 8(c,d) and 9(c,d)]. The extrapolation to the “continuum limit”, i.e. $\alpha_z \rightarrow 0$, works accurately for magnetic fields up to $B = 100 T_K$ [see Figs. 6(a) and 7(a)]. In particular, it is consistent across conventional or adaptive broadening, and in the case of the Kondo model, one also sees excellent agreement of the peak position with accurate DMRG simulations [Fig. 6(a) with data reproduced from Ref. 22]; the difference in the remaining line shape is attributed to the drastically finer discretization grid employed in the DMRG simulations as compared to the $\Lambda = 2$ for the NRG data here. For $B \gg 100 T_K$, such as $B = 10^3 T_K$ in Figs. 6(a) and 7(a), the extrapolation is less reliable leading to larger error bars. The reason for this is that the line-shape becomes less peak shaped, but more and more step-like which increases the uncertainty in the determination of the position of the peak-maximum.

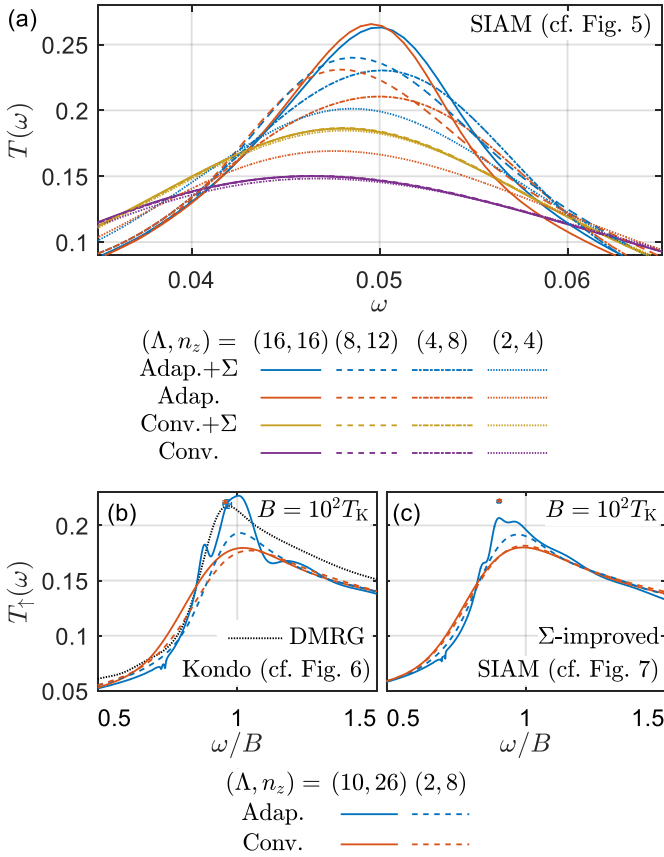


FIG. 10. Dependence of T -matrices on $\Lambda \in [2, 16]$, for the models discussed in Secs. IV B–IV C and Figs. 5–7. Here we use $\alpha = 2$, and for comparable accuracy across the wide range of Λ , we employ an energy-based truncation with $E_{\text{trunc}} = 10$, throughout. (a) Zoom into the Hubbard side peaks of the SIAM at $B = 0$ (see Fig. 5 for system parameters). Here we choose different pairs of (Λ, n_z) with a constant ratio $\log(\Lambda)/n_z$. This implies the same spectral resolution within the conventional broadening scheme in that the brown and purple lines (lower two rows in the legend) (nearly) lie on top of each other. Panels (b) and (c) show the T -matrix for (b) the Kondo and (c) the SIAM at large magnetic field ($B = 10^2 T_K$; see Figs. 6 and 7 for system parameters, respectively). Here again $\log(\Lambda)/n_z = \log(10)/26 \simeq \log(2)/8$ was chosen comparable. Note that by truncating with respect to energy ($E_{\text{trunc}} = 10$) rather than fixed number of states, the curves of $\Lambda = 2$ here slightly differ from the ones in Figs. 5–7. For comparison, we again also plot the extrapolated peak position and height (blue and red crosshairs) and the DMRG data (black dotted line), adapted from Figs. 6(a) and 7(a).

D. Larger Λ

In the previous Sections, we have used constant $\Lambda = 2$, a typical choice for NRG simulations of single-band impurity models, and kept $N_{\text{keep}} = 500$ or 2000 multiplets to demonstrate well-converged results. For multi-band problems, however, this choice of $\Lambda = 2$ is no more practical since the required number of multiplets N_{keep} in-

creases exponentially with the number of bands, and the computational cost scales like $\mathcal{O}(N_{\text{keep}}^3)$. This problem can be partly ameliorated by using significantly larger Λ , where the energy scales of the Wilson chain sites $\sim \Lambda^{-n/2}$ are better separated. Then the entanglement in the ground state of the Wilson chain is lowered¹⁴, with the effect that a significantly smaller N_{keep} suffices for well-converged results. Accordingly, $4 \lesssim \Lambda \lesssim 10$ is frequently used to simulate multi-band models accurately and feasibly. For such larger Λ , z -averaging is absolutely crucial to cancel out oscillatory behavior due to enhanced discretization artefacts.²

Here we demonstrate that, depending on the situation, one can achieve nearly comparable spectral resolution for Λ as large as 16. This is further supported by the adaptive broadening where the resolution enhancement is more significant for larger Λ . For this, we revisit the systems considered in Secs. IV B and IV C. In Fig. 10(a), we depict the Hubbard side peaks of the SIAM in the absence of magnetic field for different choices of (Λ, n_z) while keeping $\log(\Lambda)/n_z$ constant to ensure comparable spectral resolution. Indeed, the conventional broadening results in hardly distinguishable curves (brown and purple lines). However, when turning on the adaptive broadening, this further resolves the Hubbard side peaks with increasing Λ . Specifically, for Λ as large as $\Lambda = 16$, (i) the curves are still smooth without any discretization blips, and (ii) the adaptively broadened curves already show comparable peak shape with and without self-energy improvement. This suggests that the peak height is converged for these curves!

In Fig. 10(b) and (c), we show the split Kondo peaks by $B = 10^2 T_K$ for the Kondo model and the SIAM, respectively. By again choosing comparable $\log(\Lambda)/n_z$, the conventionally broadened curves for different Λ are nearly on top of each other. In contrast, the adaptively broadened curves for larger $\Lambda = 10$ again show enhanced resolution, even though here for $B \gg T_K$ at the price of more pronounced discretization artefacts. While this may not come as a surprise – after all we are using a hugely crude discretization based on $\Lambda = 10$ – one can still observe that aside from discretization related blips, the mean of the resulting curve still moves around a consistent overall lineshape. In particular, the data in Fig. 10(b-c) is still consistent with the $\alpha \rightarrow 0$ extrapolated peak height (symbols) or the DMRG data [black dotted line in panel (b)] replicated from Figs. 6 and 7. Also in Fig. 10(b), the height of the plateau for $\omega > B$ is consistent within the NRG *in the entire range* $\Lambda \in [2, 10]$. Therefore we believe the NRG data is more reliable for $\omega > B$ than the replicated DMRG data which itself may have suffered from inaccuracies in a numerically necessarily unstable deconvolution scheme.

We conclude this Section with a few technical remarks. In order to compare the data for different Λ at the same footing with similar accuracy, the state space truncation within the NRG² proceeds along an energy-based threshold $E_{\text{trunc}} = 10$ with adaptively varying number of kept

multiplets N_{keep} , rather than a fixed N_{keep} , using the conventions adopted in Ref. 17, keeping all states without truncation for the first five NRG iterations. For example, in Figs. 10 (b-c) where we have used $U(1)_{\text{spin}} \otimes SU(2)_{\text{ph}}$ symmetry, the resulting number of kept states (multiplets) is $\lesssim 6700$ (2700) for $\Lambda = 2$, and $\lesssim 300$ (150) for $\Lambda = 10$, respectively. This demonstrates the clear reduction in computational cost by using larger Λ .

V. RESULTS AT FINITE T

In the previous Section we analyzed frequencies $|\omega| \gg T = 0^+$ where log-Gaussian broadening is well-suited. For frequencies $|\omega| \lesssim T$, however, this needs to be amended by a linear broadening scheme, as discussed in Sec. III earlier. In this Section, we present the results for the SIAM at three different temperature scales $T \ll T_K$, $T \sim T_K$, and $T \gg T_K$, as shown in Figs. 11-13, respectively. This is followed by a comparison to QMC data at intermediate temperatures, as well as a discussion on a systematic way to determine the optimal value of linear broadening width γ .

In Fig. 11, we depict $T(\omega)$ at finite $T \ll T_K$, where the Kondo peak height is close to the perfect transmission $T(0) \simeq 1$. Using log-Gaussian broadening only [blue solid line in Fig. 11(a)] the spectral curve shows irregular behavior at $|\omega| \ll T$ due to effectively finite chain length induced by finite T [cf. Sec. III B]. Note though, that the log-Gaussian broadened spectral data is already smooth for frequencies $\omega \geq T$. After further convolving the curve with the linear kernel δ_γ in Eq. (21), a smooth curve emerges for $\gamma = T/10$ (still very small as compared to temperature T).

At elevated temperatures $T \gtrsim T_K$, the Kondo physics becomes suppressed by thermal fluctuations. Fig. 12(a) shows that the Kondo peak height at $T \simeq 2T_K$ is almost halved from the value at $T = 0^+$. At even higher temperature $T \simeq 100T_K$, the Kondo physics is fully suppressed, leaving behind only the two Hubbard side peaks, as illustrated in Fig. 13.

We observe that the discrete data \bar{A}/ω shows a pronounced spread along σ_k as $|\omega_k|$ decreases below T : while the spread appears only at $|\omega_k| \lesssim T/3$ for $T \ll T_K$ [Fig. 11(b)], the spread becomes even more pronounced over all $|\omega_k| \leq D$ for $T \gg T_K$ [Fig. 13(b)]. Given an interacting model, this spread in broadening width σ_k naturally tends to smear out spectral data on the energy scale of temperature.

Next we analyze how the low-frequency region of $T(\omega)$ changes with γ . This is illustrated in Figs. 12(b) and 13(d) for $T \sim T_K$ and for $T \gg T_K$, respectively. For both cases, $\gamma/T = 0.1$ sufficiently smooths the curve, and at the same time minimizes overbroadening (brown and purple lines). In contrast, the curves of $\gamma/T < 0.1$ show discretization-related oscillations [red line in Fig. 12(b), red and blue lines in Fig. 13(d)]. Meanwhile, for $\gamma/T > 0.1$, the curve segments over the interval

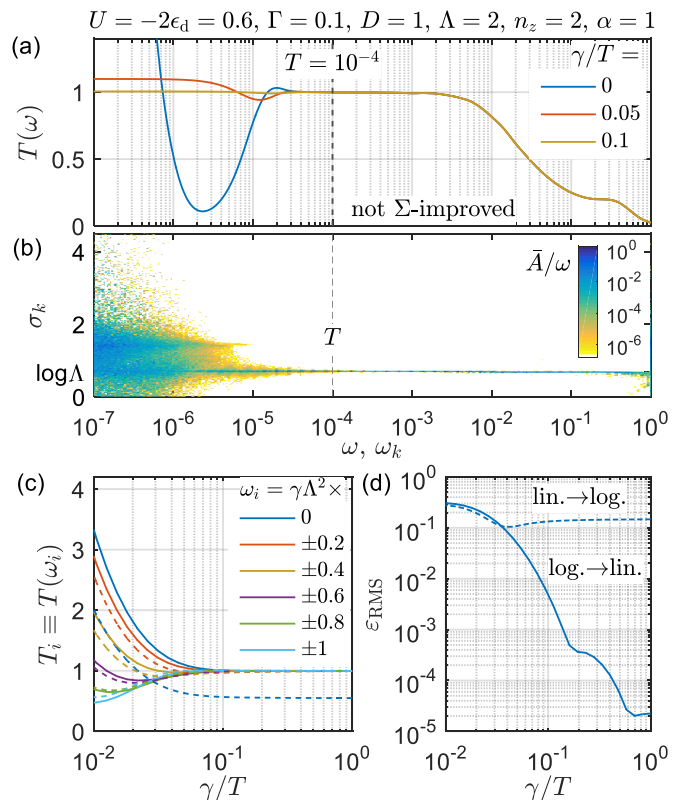


FIG. 11. T -matrix of the SIAM at finite $T \ll T_K$. (a) Broadened curves for different γ and (b) binned discrete data \bar{A}/ω for $T(\omega)$. Contrary to the confined distribution of \bar{A}/ω at $T \lesssim \omega_k \lesssim T_K$ and $\sigma_k \simeq \log \Lambda$, the weights at $|\omega| \ll T$ spread widely along σ_k . This leads to distinct irregular behavior in $T(\omega)$ at $|\omega| \ll T$ after the logarithmic Gaussian broadening [blue solid line in (a)]. The secondary convolution with width $\gamma \lesssim T$ smears out sharp fluctuations without the blip artefact, keeping features at higher ω untouched [red and brown solid lines in (a)]. (c) Spectral function values $T_i \equiv T(\omega_i)$ at frequencies $\omega_i = \gamma \Lambda^2 \times \{-1, -0.8, -0.6, \dots, 1\}$ vs. γ/T (see text). (d) Error ϵ_{RMS} of quadratic polynomial fit vs. γ/T [see Eq. (24)]. In (c,d), solid lines are obtained by applying first the log-Gaussian and then the linear broadening kernels, as in Eq. (16). In comparison, dashed lines are obtained by the opposite order of broadening; the order of broadening kernels is essential to obtain smooth curves at $|\omega| \lesssim T$ [cf. Sec. III B].

$|\omega| < T/2$ are overall shifted (relative to the curves for $\gamma/T \leq 0.1$) hence indicating the onset of overbroadening (green lines).

1. Comparison to QMC data

At intermediate temperatures $T \sim T_K$, we can compare our NRG result with recent state-of-the-art quantum Monte Carlo (QMC) calculation.²⁵ The results are presented in Fig. 12(a) at $T = D/30 \simeq 2T_K$. Though our NRG result mostly lies within the error bar of the QMC result, at $\omega = 0$ the Kondo peak height of the NRG is

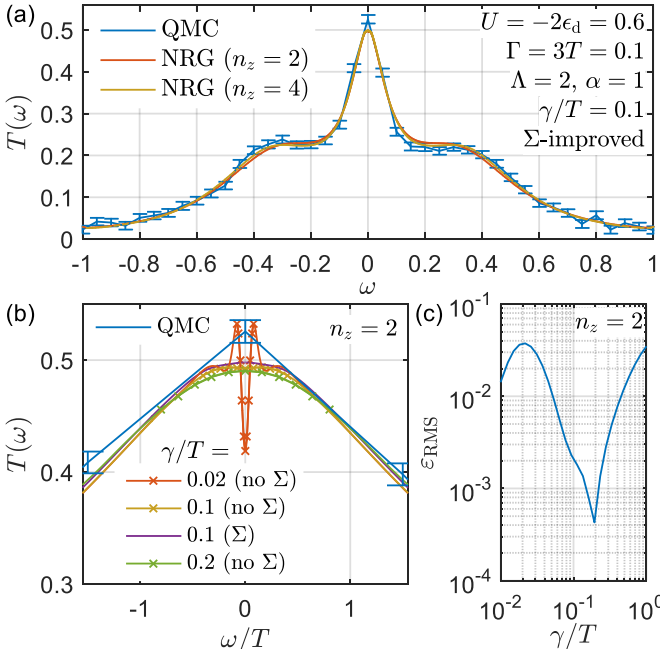


FIG. 12. T -matrix of the SIAM at $T = D/30 \simeq 2T_K$. (a) Comparison of NRG and quantum Monte Carlo results (data from Ref. 25) (b) Low-frequency region of $T(\omega)$ for different γ , where \times symbols are the discrete points T_i at $\omega_i = \gamma\Lambda^2 \times \{-1, -0.8, -0.6, \dots, 1\}$ vs. γ/T to estimate the smoothness of the curve at $|\omega| \sim \gamma$. (c) Error ε_{RMS} of quadratic polynomial fit for discrete points vs. γ/T [cf. Eq. (24)].

systematically about 5% lower, and thus clearly outside the QMC error bar. NRG, however, is known to produce consistent accurate results at $\omega = 0$ to within 1% at arbitrary temperature [e.g. see the perfect consistency with Friedel sum-rule at $T \ll T_K$ in Fig. 11(a)]. We speculate that the QMC may have overestimated the peak height or underestimated the error bar. Also the current setting of $U = -2\varepsilon_d$ yields the particle-hole symmetry, which appears in the T -matrix as $T(\omega) = T(-\omega)$. While the NRG accurately reproduces the symmetry, the QMC data is only barely particle-hole symmetric within its error bars. For the results in Figs. 11-13, we kept up to 500 multiplets (about 3300 states) exploiting $SU(2)$ spin and $SU(2)$ particle-hole symmetry in each step of the iterative diagonalization. For a single z -shift, the calculation of the entire spectral data took about ten minutes on an 4-core workstation. Note that in the QMC calculation the band edges of $\Gamma(\varepsilon)$ are slightly smoothed, but this smoothing does not affect the NRG result as we explicitly checked.

2. Optimal choice for linear broadening width γ

The width γ of the linear broadening that follows the log-Gaussian broadening, so far, is a parameter that needs to be tuned by hand. While sufficiently large $\gamma \lesssim T$

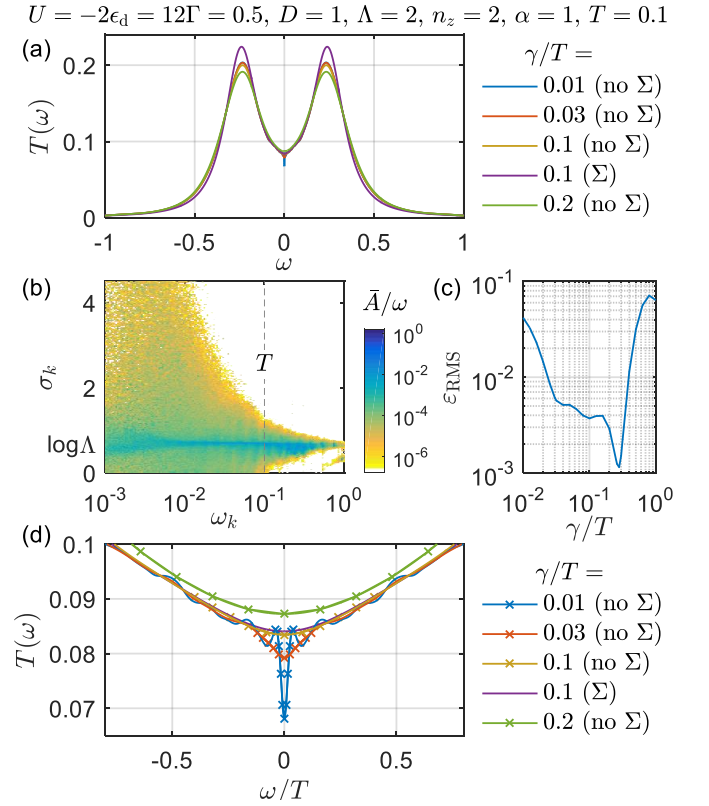


FIG. 13. T -matrix of the SIAM at large temperature ($T \simeq 100T_K$). (a) Broadened curves for various γ . Due to high temperature, the Kondo peak is completely suppressed while the Hubbard side peaks persist at $\omega = \pm U/2$. Using the self-energy (Σ) improves the spectral resolution of the Hubbard peaks. The Σ -improved curve for $n_z = 2$ at $\gamma/T = 0.1$ (purple line) shows a height of the Hubbard peaks that is comparable with a non- Σ -improved curve for $n_z = 8$ and the same $\gamma/T = 0.1$ (not shown). (b) Binned discrete data \bar{A}/ω for $T(\omega)$. While the weights at $|\omega_k| < T$ spread widely along σ_k for $T \ll T_K$ [see Fig. 11(b)], here a certain spread also appears at $|\omega_k| \gtrsim T$. (c) Same as Fig. 12(c). (d) Same as Fig. 12(b).

ensures a smooth final spectral curve, $\gamma = T$ typically already results in clear overbroadening. Ideally, γ is chosen as small as possible to just smear out discretization related irregularities at $|\omega| \ll T$ that are out of reach for the log-Gaussian broadening, but keeps the overbroadening of already smooth physical features at $|\omega| \gtrsim T$ to a minimum. The optimal choice for the linear broadening width γ for the spectral data for $|\omega| < T$ necessarily depends on the underlying physics. Hence a systematic determination of γ is desirable.

Foremost, this requires a measure to quantify “smoothness” of the data $|\omega| \lesssim T$ on a linear scale including its transition to the log-Gaussian broadening. We start from spectral data that has already been broadened in the *entire* frequency range by an adaptive log-Gaussian scheme as described earlier. Then we estimate the smoothness of the curve obtained after the linear broadening with any $\gamma \leq T$: we sample $T(\omega)$ on a linear grid of frequencies

ω_i in the close vicinity of $\omega = 0$, and check whether the sampled values $T(\omega_i)$ can be well fit by a quadratic functions. If so, $T(\omega)$ is regarded as smooth. This procedure avoids applying the linear broadening to the entire spectral range. Hence the determination of an optimal γ as outlined here, is numerically cheap.

To be specific, we consider (i) a *linear* frequency range $\omega \in [-\omega_l, \omega_l]$ with $\omega_l \equiv \gamma\Lambda^2$. (The subscript l stands for linear.) Eventually, we will demand that the broadened resulting spectral data closely follows a quadratic polynomial in this interval. By including the scale factor Λ^{n_l} with $n_l = 2$ in the definition of ω_l , the linear broadening width γ is extended to at least n_l intervals of the underlying logarithmic discretization for both positive and negative frequencies. This ensures that the analysis of the resulting smoothness clearly reaches across into the log-Gaussian broadened frequency range. (ii) Next we split this frequency range $\omega \in [-\omega_l, \omega_l]$ into a uniformly spaced linear grid ω_i of m_l frequencies $\{\omega_i\} = [-\omega_l, \dots, \omega_l]$, where we choose $m_l = 5n_l + 1 = 11$. By being odd, this includes the frequency $\omega = 0$, and by being $> 4n_l$, this ensures sufficient resolution into the underlying logarithmic discretization grid towards the log-Gaussian broadened data at $|\omega| \sim \omega_l$. (iii) We then compute the linearly broadened data $\{T_i\} \equiv T(\{\omega_i\}; \gamma)$ at the above linear grid of m_l frequencies only [see Fig. 11(c)], and (iv) perform a quadratic fit on this data (ω_i, T_i) , which results in a quadratic polynomial $\tilde{T}(\omega)$ for the data range $|\omega| \leq \omega_l$. We define the error estimate of the fit as the normalized distance of the data to this quadratic fit,

$$\varepsilon_{\text{RMS}} \equiv \frac{\sqrt{\langle \delta^2 T_i \rangle}}{\langle T_i \rangle}, \quad (24)$$

where $\langle T_i \rangle \equiv \frac{1}{m_l} \sum_{i=1}^{m_l} T_i$ is the average and $\langle \delta^2 T_i \rangle \equiv \frac{1}{m_l - 3} \sum_{i=1}^{m_l} (T_i - \tilde{T}(\omega_i))^2$ is the standard error of fitting [note that $m_l - 3$ is the statistical degree of freedom, as there are three coefficients of quadratic polynomial fitting function]. (v) The error ε_{RMS} provides the desired estimate for the smoothness of the fully broadened data for frequencies $|\omega| \lesssim T$ that now includes both, the initial log-Gaussian, as well as the subsequent linear broadening of width γ . A small value of ε_{RMS} implies that $T(\omega)$ indeed behaves quadratically within the fitting range $[-\omega_l, \omega_l]$, indicating that discretization artefacts have been satisfactorily smoothed out.

In Figs. 11(d), 12(c), and 13(c), we show the dependence of the fitting error estimate ε_{RMS} vs. γ in three different regimes $T \ll T_K$, $T \sim T_K$, and $T \gg T_K$, respectively. At $T \ll T_K$, the error ε_{RMS} monotonously decreases with increasing γ [solid line in Fig. 11(d)], due to the featureless flat behavior of $T(\omega)$ at $|\omega| \lesssim T \ll T_K$. As seen in Fig. 11(a), the spectral data is visibly smooth for $\gamma/T = 0.1$, which corresponds to $\varepsilon_{\text{RMS}} \simeq 0.002$.

The situation becomes different at higher temperatures, in that $T(\omega)$ actually has structure, e.g. curvature at $|\omega| \lesssim T$. Therefore the strong rise of ε_{RMS} towards larger γ at $\gamma/T > 0.2$ [Fig. 12(c)] and at $\gamma/T > 0.3$

[Fig. 13(c)] indicates the onset of overbroadening: given that the line shape within the linear frequency window $|\omega| \leq T$ is no longer exactly quadratic [see Figs. 12(b) and 13(d)], the fitting quality of a quadratic fit in the range $[-\omega_l, \omega_l]$ (with $\omega_l = \gamma\Lambda^2$) necessarily deteriorates with larger γ .

Conversely, the strong increase of ε_{RMS} towards small γ in Fig. 12(c) [as already also seen in Fig. 11(d)] indicates the onset of discretization artefacts due to underbroadening. In Fig. 12(c) this occurs for $\gamma/T < 0.2$. With $\gamma/T = 0.2$ still visibly overbroadened, though, due to the smallness of ε_{RMS} at $\gamma/T = 0.2$, γ can be further reduced as long as discretization artefacts are still weak. Similar to Fig. 11(d) where we estimated $\varepsilon_{\text{RMS}} \simeq 0.002$ for smooth data, the same requirement also leads to $\gamma/T = 0.1$ here.

A similar picture emerges for large temperatures as seen in Fig. 13(c): a strong increase in ε_{RMS} , for $\gamma/T > 0.3$ due to overbroadening, and for $\gamma/T < 0.03$ due to underbroadening. In the large temperature case, however, there emerges an intermediate window for $\gamma/T \in [0.03, 0.3]$ that shows more irregular behavior of ε_{RMS} yet at small values. This is interpreted as a consequence of the interplay of the underlying discrete data with the broadening as well as the intrinsic line shape of the spectral function.

Based on the above observations, we therefore suggest the following procedure to determine the optimally minimal γ : (i) Obtain the dependence ε_{RMS} vs. γ , over a wide range on a log-scale, e.g. $\gamma/T \in [0.01, 1]$. Since the evaluation of ε_{RMS} does not require the linear broadening over all frequencies, this step can be done efficiently. By analyzing its dependence, we can identify the regimes where under- or over-broadening occurs. (ii) If only the underbroadening behavior appears [e.g. $T \ll T_K$ as in Fig. 11(d)], choose the value of γ/T at which ε_{RMS} passes through a certain threshold, e.g. 0.002. So we have chosen $\gamma/T = 0.1$ in Fig. 11(d). (iii) If the underbroadening behavior appears directly next to the overbroadening behavior [e.g. $T \sim T_K$ as in Fig. 12(c)], there will be two values of γ/T at which ε_{RMS} passes through the threshold, e.g. 0.002. We choose the smaller γ , since the larger one clearly overbroadens the curve; thus $\gamma/T = 0.1$ is chosen in Fig. 11(d) as well. (iv) If there exists a more irregular region between the under- and over-broadening regimes [e.g. $T \gg T_K$ as in Fig. 13(d)], take the geometric mean (or the midpoint on a log-scale, equivalently) of the smallest overbroadening γ/T and the largest underbroadening γ/T to stay equally far from either side. For the example of Fig. 13(d), these two values are $\gamma/T \simeq 0.03$ and 0.3, respectively. Incidentally, this again results in an optimal $\gamma/T \simeq 0.1$ at slightly enhanced $\varepsilon_{\text{RMS}} \simeq 0.003$. As seen in Fig. 13(a,d), this trades off the shift of the curve segment due to overbroadening against the oscillation due to underbroadening.

VI. SUMMARY

We have developed an adaptive scheme which broadens each discrete spectral weight individually based on its position's sensitivity on z -shifts in the underlying logarithmic discretization. For frequencies $|\omega| \lesssim T$ we have developed a systematic scheme to keep the required linear broadening of width γ to a minimum.

The additional computational cost for the adaptive broadening is minor: (i) Only the matrix elements of the perturbation dH/dz need to be computed to estimate the broadening width. (ii) The discrete spectral data then is collected on a 2-dimensional array, i.e. with dimensions frequency ω_k and broadening σ_k . (iii) The actual broadening is part of the post-analysis of the fdm-NRG run. Its cost is linear proportional to the number n_σ of bins in the broadening σ_k , where in practice a linear grid of $n_\sigma \simeq 50$ bins should suffice for a linear range $\sigma \in [0, 2] \times \log \Lambda$.

The adaptive broadening presented here systematically improves spectral resolution. With increasing n_z , it converges much more quickly to the analytically known line shapes of non-interacting models than the conventional broadening. Yet also for interacting models, the adaptive broadening converges faster to the ‘‘continuum limit’’. In the limit of infinite z -averaging, i.e. $n_z \rightarrow \infty$, the adaptive approach necessarily coincides with the conventional approach. However, the infinite n_z limit is not accessible within the NRG (and moreover is biased by the existence of the band edges, see Sec. IID). The adaptive scheme presented in this paper systematically improves spectral resolution from dynamical NRG data at finite $n_z \geq 2$. Therefore the proposed adaptive broadening should benefit two widely used applications of the NRG: (i) DMFT calculations in the quest to deal with structured bath hybridization functions and, quite generally, (ii) multi-band (effective) impurity calculations to obtain maximal spectral resolution at necessarily larger coarse graining in energy.

VII. ACKNOWLEDGEMENT

We thank to Jan von Delft for fruitful discussion, Emanuel Gull for providing us with his QMC data, and Theo Costi for useful feedback. S. L. acknowledges support from the Alexander von Humboldt Foundation and the Carl Friedrich von Siemens Foundation. A. W. was supported by DFG (Nanosystems Initiative Munich, and Grant No. WE4819/2-1).

Appendix A: Logarithmic discretization

In this appendix we discuss the numerical calculation of the derivatives of hopping amplitudes dt_n/dz and of onsite energies $d\varepsilon_n/dz$. This analysis proceeds independently for each flavor ν . Hence, for simplicity, we skip the flavor index in the following discussion.

For simplicity, we also focus on the case that the impurity and the bath are coupled via the quadratic hybridization H_{cpl} with the hybridization function $\Gamma(\omega)$ as in the SIAM in Eq. (4), but our argument is easily extendible to the Kondo model. As usual within the NRG, we define the logarithmic discretization intervals symmetrically for positive and negative energies, i.e. $I_{k,+}^{(z)} \equiv (\epsilon_{k+1}^{(z)}, \epsilon_k^{(z)})$ and $I_{k,-}^{(z)} \equiv [-\epsilon_k^{(z)}, -\epsilon_{k+1}^{(z)}]$, with

$$\epsilon_k^{(z)} = \begin{cases} D, & k = 0, \\ D\Lambda^{-k+1-z}, & k > 0. \end{cases} \quad (\text{A1})$$

In the process of coarse-graining, we replace the bath continuum within each interval $I_{ks}^{(z)}$ with $k = 0, 1, 2, \dots$ and $s \in \{+, -\}$ by a single discrete level at energy $\xi_{ks}^{(z)}$ which couples to the impurity with amplitude $t_{ks}^{(z)} = (\frac{\gamma_{ks}^{(z)}}{\pi})^{1/2}$. The total hybridization of the discrete levels represents the hybridization of the continuum still, since

$$\int \Gamma(\epsilon) d\epsilon = \sum_{ks} \underbrace{\int_{I_{ks}^{(z)}} \Gamma(\epsilon) d\epsilon}_{\equiv \gamma_{ks}^{(z)}}, \quad (\text{A2})$$

which defines $\gamma_{ks}^{(z)}$. The continuum limit may be restored by z -averaging over $n_z \rightarrow \infty$ z -shifts that are uniformly distributed within $z \in (0, 1]$, i.e. $\frac{1}{n_z} \sum_z \rightarrow \int_0^1 dz$. With focus on the non-interacting bath only, the energy $\xi_{ks}^{(z)}$ then needs to satisfy¹⁰

$$\Gamma(\xi_{ks}^{(z)}) = \gamma_{ks}^{(z)} \left/ \left| \frac{d\xi_{ks}^{(z)}}{dz} \right| \right., \quad (\text{A3})$$

which is a differential equation in the continuous variable $x \equiv k + z \in [0, \infty]$.

Via coarse-graining in energy space, the continuous star Hamiltonian $H_{\text{cpl}} + H_{\text{bath}}$ in Eq. (2) becomes the discrete star Hamiltonian $H_{\text{star}} = \psi_{\text{star}}^{(z)\dagger} \mathbf{H}_{\text{star}}^{(z)} \psi_{\text{star}}^{(z)}$ where $\psi_{\text{star}}^{(z)} \equiv (d, a_{0+}^{(z)}, a_{1+}^{(z)}, \dots, a_{0-}^{(z)}, a_{1-}^{(z)}, \dots)^T$ with $a_{ks}^{(z)}$ the annihilation operator of the discretized bath level (ks) for a given z , and

$$\mathbf{H}_{\text{star},\nu}^{(z)} = \begin{pmatrix} 0 & t_{0+}^{(z)} & t_{1+}^{(z)} & \dots & t_{0-}^{(z)} & t_{1-}^{(z)} & \dots \\ t_{0+}^{(z)} & \xi_{0+}^{(z)} & & & & & \\ t_{1+}^{(z)} & & \xi_{1+}^{(z)} & & & & \\ \vdots & & & \ddots & & & \\ t_{0-}^{(z)} & & & & \xi_{0-}^{(z)} & & \\ t_{1-}^{(z)} & & & & & \xi_{1-}^{(z)} & \\ \vdots & & & & & & \ddots \end{pmatrix}. \quad (\text{A4})$$

Here ‘‘star’’ means a star-shaped tree geometry of how the impurity and the bath levels are coupled; the impurity couples to the bath levels and there is no direct coupling between the bath levels. Then by Lanczos

tridiagonalization with the starting vector $[1, 0, 0, \dots]^T$, i.e. leaving the impurity level d as it is, the star Hamiltonian in Eq. (A4) can be exactly mapped onto a chain geometry, $H_{\text{chain}}^{(z)} \equiv \psi_{\text{chain}}^{(z)\dagger} \mathbf{T}^{(z)} \psi_{\text{chain}}^{(z)}$, with $\psi_{\text{chain}}^{(z)} \equiv (d, f_0^{(z)}, f_1^{(z)}, f_2^{(z)}, \dots)^T$ and the tridiagonal Hamiltonian matrix

$$\mathbf{T}^{(z)} = [\mathbf{U}^{(z)}]^\dagger \mathbf{H}_{\text{star}}^{(z)} \mathbf{U}^{(z)} \quad (\text{A5})$$

$$= \begin{pmatrix} 0 & t_0^{(z)} & & & \\ t_0^{(z)} & \varepsilon_0^{(z)} & t_1^{(z)} & & \\ & t_1^{(z)} & \varepsilon_1^{(z)} & t_2^{(z)} & \\ & & t_2^{(z)} & \varepsilon_2^{(z)} & \ddots \\ & & & \ddots & \ddots \end{pmatrix}. \quad (\text{A6})$$

By construction, the discrete intervals (ks) depend on the underlying z -shift. Therefore also $\psi_{\text{star}}^{(z)}$ and subsequently also $\psi_{\text{chain}}^{(z)}$ refer to a z -dependent coarse-grained basis set. From the point of view of the impurity in the NRG, however, the set $\{f_n\}$ simply refers to a set of one-particle states. In this sense, the z -dependence in $\psi_{\text{chain}}^{(z)}$ is irrelevant and can be ignored.

Therefore by only considering the z -dependence of the tridiagonal matrix $\mathbf{T}^{(z)}$, the perturbation dH/dz translates into $d\mathbf{T}/dz$. Based on the defining equations (A2–A6), we therefore simply compute

$$\frac{d\mathbf{T}^{(z)}}{dz} \simeq \frac{1}{\delta z} \left(\mathbf{T}^{(z+\delta z)} - \mathbf{T}^{(z)} \right) \quad (\text{A7})$$

This perturbation simply consists of the numerical derivatives $d\varepsilon_n/dz$ and dt_n/dz which enter the diagonal and first off-diagonal in $d\mathbf{T}/dz$, respectively. These, however, are numerical derivatives that need to be based on two different Lanczos tridiagonalizations with slightly offset z -shifts. In practice, we chose $\delta z = 0.01/n_z$. Note that the perturbation $d\mathbf{T}/dz$ clearly cannot be simply related to the differentiation of $d\xi_{ks}/dz$ and dt_{ks}/dz in the star geometry since the unitary transformation $\mathbf{U}^{(z)}$ itself is z -dependent.

For any hybridization function $\Gamma(\omega)$ that is finite at $\omega = 0$, the asymptotic behavior for large n for the hopping amplitudes is $t_n^{(z)} \propto 1/\Lambda^{\frac{n}{2}+z}$ and therefore $(dt_n^{(z)}/dz)/t_n^{(z)} = d \log(t_n^{(z)})/dz \simeq -\log \Lambda$ [eventually, this needs to be multiplied by the global factor $1/n_z$ to get the full perturbation; cf. Eq. (17b)]. The onsite energies $\varepsilon_n^{(z)}$ have nontrivial asymptotic behavior that decays

at least as Λ^{-n} , unless the particle-hole symmetry enforces $\varepsilon_n^{(z)} = 0$.

Appendix B: Equation (19) in case of degeneracy

For the estimate of the broadening width of discrete spectral data based on its sensitivity on z -shifts, we made use of the Hellmann-Feynmann theorem in Eq. (19) in the main text. Here we address the implications of (accidental) degeneracy in the energy eigenstates.

Degeneracy of eigenstates typically occurs due to symmetry such as particle number conservation, particle-hole symmetry, total spin conservation, etc. In practical NRG calculations, these symmetries are fully exploited to strongly reduce numerical cost in terms of memory consumption and CPU time.²¹ Accidental degeneracy can be neglected, since this always may be removed by an infinitesimal external perturbation, which in a numerical setting may be interpreted as numerical noise that always weakly lifts exact accidental degeneracy anyway.

Therefore degenerate eigenstates typically arise due to symmetry. As such they are (i) part of the same multiplet if the full symmetry setting includes non-abelian symmetries (e.g. degenerate states within a given symmetry multiplet, say, of some total spin S) or (ii) distinguishable by different quantum numbers (such as spin-component S_z) if a reduced symmetry setting is used for the simulation itself. In either case, the matrix elements of dH/dz will be block-diagonal with respect to symmetry by the Wigner-Eckart theorem, since the perturbation dH/dz relates to a scalar Hamiltonian (note that z -shifts do not break the symmetry of the original Hamiltonian).

Consequently the application of the Hellmann-Feynmann is legitimate, since degenerate eigenstates in different symmetry sectors are distinguishable, i.e. they do not mix. Conversely, degeneracy within a given symmetry multiplet space has always a diagonal matrix representation, since the Clebsch-Gordan coefficients out of the Wigner-Eckart theorem for a scalar operator are always proportional to an identity matrix. Hence the perturbation will not mix in between different states of the same multiplet since symmetry is preserved.

Overall, therefore this justifies that we can use the energy eigenstates $|E_i\rangle$ directly obtained from the iterative diagonalization in Eq. (19) without having to worry about degenerate subspaces.

* s.lee@lmu.de

† andreas.weichselbaum@lmu.de

¹ K. G. Wilson, Rev. Mod. Phys. **47**, 773 (1975).

² R. Bulla, T. A. Costi, and T. Pruschke, Rev. Mod. Phys. **80**, 395 (2008).

³ A. Georges, G. Kotliar, W. Krauth, and M. J. Rozenberg,

Rev. Mod. Phys. **68**, 13 (1996).

⁴ R. Bulla, Phys. Rev. Lett. **83**, 136 (1999).

⁵ K. M. Stadler, Z. P. Yin, J. von Delft, G. Kotliar, and A. Weichselbaum, Phys. Rev. Lett. **115**, 136401 (2015).

⁶ A. Weichselbaum and J. von Delft, Phys. Rev. Lett. **99**, 076402 (2007).

- ⁷ R. Bulla, T. A. Costi, and D. Vollhardt, *Phys. Rev. B* **64**, 045103 (2001).
- ⁸ M. Yoshida, M. A. Whitaker, and L. N. Oliveira, *Phys. Rev. B* **41**, 9403 (1990).
- ⁹ V. L. Campo and L. N. Oliveira, *Phys. Rev. B* **72**, 104432 (2005).
- ¹⁰ R. Žitko and T. Pruschke, *Phys. Rev. B* **79**, 085106 (2009).
- ¹¹ A. Freyn and S. Florens, *Phys. Rev. B* **79**, 121102 (2009).
- ¹² F. B. Anders and A. Schiller, *Phys. Rev. Lett.* **95**, 196801 (2005).
- ¹³ F. B. Anders and A. Schiller, *Phys. Rev. B* **74**, 245113 (2006).
- ¹⁴ A. Weichselbaum, *Phys. Rev. B* **86**, 245124 (2012).
- ¹⁵ T. A. Costi, *Phys. Rev. Lett.* **85**, 1504 (2000).
- ¹⁶ R. Bulla, A. C. Hewson, and T. Pruschke, *J. Phys.: Condens. Matter* **10**, 8365 (1998).
- ¹⁷ A. Weichselbaum, *Phys. Rev. B* **84**, 125130 (2011).
- ¹⁸ K. M. Stadler, Master's thesis, Ludwig-Maximilians-Universität München (2013).
- ¹⁹ Ž. Osolin and R. Žitko, *Phys. Rev. B* **87**, 245135 (2013).
- ²⁰ M. Hanl and A. Weichselbaum, *Phys. Rev. B* **89**, 075130 (2014).
- ²¹ A. Weichselbaum, *Ann. Phys.* **327**, 2972 (2012).
- ²² A. Weichselbaum, F. Verstraete, U. Schollwöck, J. I. Cirac, and J. von Delft, *Phys. Rev. B* **80**, 165117 (2009).
- ²³ A. Rosch, T. A. Costi, J. Paaske, and P. Wölfle, *Phys. Rev. B* **68**, 014430 (2003).
- ²⁴ M. Garst, P. Wölfle, L. Borda, J. von Delft, and L. Glazman, *Phys. Rev. B* **72**, 205125 (2005).
- ²⁵ G. Cohen, E. Gull, D. R. Reichman, and A. J. Millis, *Phys. Rev. Lett.* **112**, 146802 (2014).